Search for stopped long-lived particles produced in pp collisions at 8 TeV at CMS

DISSERTATION

Presented in Partial Fulfillment of the Requirements for the Degree Doctor of Philosophy in the Graduate School of The Ohio State University

By

Marissa Rodenburg, M.S., B.S.

Graduate Program in Physics

The Ohio State University

2014

Dissertation Committee:

Professor L. Stanley Durkin, Advisor

Professor Christopher Hill

Professor Yuri Kovchegov

Professor Greg Lafyatis

Abstract

At the Large Hadron Collider counter-rotating proton beams are collided at $\sqrt{s} =$ 8 TeV. The Compact Muon Solenoid (CMS) is used to measure the energies and charges of the resulting cascade of particles produced in these collisions. This search focuses on the observation of massive, long-lived particles, such as the gluino, that would suggest new physics beyond the Standard Model. A custom trigger is used to probe time periods during which no proton collisions occur, thereby eliminating most backgrounds to the signal. The remaining backgrounds resulting from cosmic rays, beam-related effects, and instrumental noise, are further reduced using a series of sophisticated selection cuts. Candidate events passing all selection cuts are analyzed using a counting experiment and limits are placed on the cross sections and masses of the gluino and the supersymmetric top quark.

I would like to dedicate my dissertation to my amazing family. To my father, Robert Rodenburg, who raised me from an early age to be curious about the world around me, and to question the very fundamental workings of the universe. To my mother, Patti Rodenburg, who taught me the foundations of engineering by sharing her many talents as a seamstress when I was a child. To my sister, Katie Rodenburg, whose love and wisdom has motivated me to accomplish my lifelong dream of pursuing a Ph.D. in physics. To my youngest sister, Lisa Rodenburg, whose incredible wealth of humor has kept my spirit high through this process.

Vita

2008	B.S. Physics & Computer Science, University of Washington
2008 - 2010	Teaching Assistant, The Ohio State University
2010	Masters of Physics, The Ohio State University
2008 - present	Research Assistant, The Ohio State University

Publications

CMS Collaboration. "Search for stopped long-lived particles produced in pp collisions at $\sqrt{s} = 7$ TeV ". Journal of High Energy Physics 2012(8), 132(2012).

Fields of Study

Major Field: Physics

Table of Contents

List of Figures

Figure **Page**

List of Tables

Table **Page**

Chapter 1
Introduction

The study of particle physics has provided scientists with deep insights into the construction and behavior of the universe. Over the course of the 20th century, physicists discovered a incredible abundance of particles, first with the electron, proton, and neutron, and then with more exotic flavors of matter. These discoveries prompted the development of what is now known as the Standard Model. This theory describes the interactions between all observed particles and was also successful in reducing the hundreds of observed composite particles, or bound states, to a small set of fundamental particles including twelve spin-1/2 particles known as fermions and four vector bosons that act as force-carriers. In addition to these, theorists also predicted the existence of a scalar boson, known as the Higgs. The Standard Model has been highly successful and rigorously proven by experiments conducted by particle physicists over the course of its evolution.

The latest experiment used to test the Standard Model is the Large Hadron Collider (LHC). The LHC is the largest particle accelerator built to date and is situated on the border between France and Switzerland. It was designed to drive two proton beams through a 27 km circumference ring at energies up to 14 TeV, resulting in the production of all varieties of known matter. It also provides an opportunity to observe new flavors of matter as yet undetected in any terrestrial particle physics

experiment to date. The observation of such particles is conducted using detectors placed around the circumference of the ring, including two general purpose detectors: the Compact Muon Solenoid (CMS) and A Toroidal LHC Apparatus (ATLAS). These detectors allow physicists to observe the production and decay of particles produced in the proton proton collisions with extremely high precision. Operating since 2008, the LHC has had great success in confirming the Standard Model, including making the first observations of the elusive Higgs boson [2] [3].

Though the Standard Model has been very successful in describing the interactions of matter, it also presents scientists with an range of problems including theoretical inadequacies such as the loop corrections of the Higgs mass, the inability to account for the gravitational force and its relatively tiny coupling, the lack of an explanation for dark matter or energy, and the lack of explanation of non-zero neutrino masses. These open problems motivate the search for physics beyond the Standard Model. One popular resolution for these issues are Supersymmetric theories (SUSY), which extend the SM and predict the existence of a new class of SUSY particles. Many searches are being conducted at the LHC for evidence of these.

The analysis described herein is one such search. A variety of SUSY theories predict the existence of heavy, quasi-stable particles that could be produced in pp collisions at the LHC. These particles would have lifetimes much longer than other SM particles, providing a distinct signature of new physics. One particular theory, Split Supersymmetry, gives rise to heavy long-lived gluinos ($\tilde{g}$) whose decays are suppressed by the large mass splitting with supersymmetric quarks. Gluinos could theoretically be pair-produced at the LHC with values of $\beta \equiv v/c$ low enough to allow them to stop within the body of the CMS detector where they will wait to decay at a later time, which could be as long as months later. This analysis is designed specifically to look for such decays by searching within time windows after pp collisions, which

would obscure the decay signature. Though this technique prevents contamination of the data from the usual Standard Model backgrounds, the search must contend with other sources of background including cosmic rays, beam-related effects, and instrumental noise.

Chapter 2 provides a description of the Standard Model as it currently stands. I will also discuss potential extensions to the SM that make predictions of long-lived particles that could be observed in the stopped particle search. Chapter 3 discusses the LHC apparatus and the technologies used in the experimental design of the CMS detector. In Chapter 4, I will introduce the software I developed to detect a particular kind of beam-related background known as beam halo. This project was undertaken in tandem with the stopped particle analysis to provide the wider CMS community a method to exclude events contaminated by beam halo. Finally, Chapter 5 will provide a rigorous description of the stopped particle search and its results.

Chapter 2
Theory

The Standard Model (SM) provides a theoretical framework to describe the physical properties and interactions between elementary particles and forces (with the exception of gravity). Developed over the last century, the SM has been tested to high accuracy using a variety of experiments, including those performed at large particle accelerator facilities such as the LHC. The theory was developed to describe the behavior of three categories of fundamental particles: fermions, the elementary particles with mass and half-integer spin; vector bosons, particles with integer spin that act as force carriers; and the Higgs boson, a scalar particle which imbues these fundamental particles with mass. In this section, I will discuss the foundations of the Standard Model, as well as its limitations. These limitations, particularly the hierarchy problem, are the driving force behind searching for new physics not described by the SM.

2.1 Standard Model

The three fundamental forces described by the Standard Model are electromagnetism, the weak force, and the strong force.

The strong force is responsible for interactions between particles possessing color charge, mediated by the gluon. Within the Standard Model, the only color-charged

particles are the quarks and the gluons. There are six flavors of quarks, each possessing a single color charge (red, blue, or green), half-integer spin, and electric charge in multiples of 1/3 e. There are 8 flavors of gluons, all electrically neutral. Each flavor contains a combination of color, anti-color pairs. The theory of quantum chromodynamics (QCD) describes these interactions. QCD has two unique properties: color confinement and and asymptotic freedom. Color confinement is the requirement that all bound states (known as hadrons) appear color-neutral outside their boundaries, i.e. there is no color field observed beyond the borders of the hadron. This bars the observation of free quarks or gluons. Asymptotic freedom is a property in which the strong force becomes increasingly weaker as the distance between color-charged particles decreases. Thus, within a bound state, the composite quarks and gluons are essentially free particles, but any attempts to separate them results in the force between the particles (and thus the energy stored in the bonds) to rapidly increase in magnitude. At distances on the order of 1 fm, the energy stored in the bound states become sufficient to pair-produce quarks and gluons out of the vacuum, resulting in the creation of additional color-neutral hadrons.

With the exception of the proton, which appears to be completely stable, and the neutron, which has a free lifetime of $\sim$14 minutes, hadrons are unstable particles that typically have short lifetimes and often can only be observed by their decays. The vast majority of the observed mass in the universe is comprised of two hadrons: the proton and neutron, though more exotic hadrons containing more massive quarks are regularly produced in high energy interactions such as those at the LHC. At high energies, hadrons appear as jets. In addition to the two or three composite quarks (bound states known as mesons and baryons, correspondingly), cascades of secondary quarks are produced out of the vacuum forming a stream of strongly-interacting particles. These jets are highly boosted with a total energy much greater than the mass

of the composite particles, and so appear as narrow cascades traversing the detector. Jets may undergo decay processes which also produce leptonic byproducts. Measuring the nuclear and electromagnetic interactions of jets with matter in a detector allow experimentalists to determine the energy of the jets. This process of measuring hadronic interactions with the CMS detector is a central piece of the stopped particle search.

The electromagnetic force comes to dominate at longer ranges, outside the color fields of the strong force. Electromagnetic interactions occur between any electrically charged particle and are mediated by the electrically-neutral, massless photon. In addition to charged hadrons, the electromagnetic force also describes interactions with a class of particles known as leptons. There are three massive leptons described by the Standard Model. In order of increasing mass, the charged leptons are the electron, the muon, and the tau. Each of these carry a charge equal to $1e$ and have spin 1/2. Each massive lepton also has a corresponding neutrino. These are electrically neutral and thus do not interact with matter electromagnetically. Recently, neutrino oscillations have been observed experimentally, and so they must be massive, though their masses are extremely small (on the order of a few eV). Of particular interest to the stopped particles is the muon. With a mass of 105 MeV, approximately 200 times that of the electron, muons are not as easily perturbed by interactions with matter, meaning they lose energy at a much lower rate and thus are not stopped as easily. This becomes critical in the search for stopped particles as two of the primary sources of background are relativistic muons generated by sources outside pp collisions. Though the rate of energy loss for muons is comparatively small, they can leave energy deposits within the body of the detector, specifically in the densest regions, via ionization and Bremsstrahlung. The ionization energy of a muon within the CMS detector are small (on the order of 2 GeV), but photons emitted via Bremsstrahlung can have much

higher energies, and when emitted within the calorimeters, these energy deposits can mimic the expected signal of a jet.

The weak interaction is several orders of magnitude weaker than electromagnetism (hence the name), and is only effective at short ranges. Weak interactions affect all particles of half-integer spin and is mediated by the massive and short-lived $W^{\pm}$ and Z bosons. The theory of weak interactions was initially developed to describe nuclear beta decay. The theory also led to the proposition of massless, electrically neutral particles that carried the missing energy from nuclear decays, thereby preserving energy conservation (as mentioned previously, these neutrinos were later determined to be massive, though there is nothing in the theoretical description of the weak force that requires this). Though neutrinos do not participate in the strong or electromagnetic interactions, they are active participants in flavor-changing observed in all other fermions. When fermions exchange W bosons, they change flavors (such as a down quark becoming an up quark or a muon decaying to an electron and two neutrinos) at least one neutrino is absorbed or emitted. The Z boson is responsible for the exchange of energy between two fermions due to inelastic scattering of two weakly interacting particles. The short range of such interactions led to the prediction of massive force mediators, necessitating a mechanism to imbue the W and Z with mass. Because these bosons have such a large mass (80 GeV and 91 GeV, respectively), weak interactions are highly suppressed and typically require the bosons mediating the interactions to be off-shell.

A proposed means of providing mass to the W and Z bosons is the Higgs mechanism. The theory proposes a Higgs field that spontaneously breaks the symmetry of the electroweak sector. At energies below the spontaneous symmetry breaking threshold, the Higgs field effectively "slows down" gauge bosons, imbuing them with a finite mass required for the short range of the weak interactions. The Higgs potential is

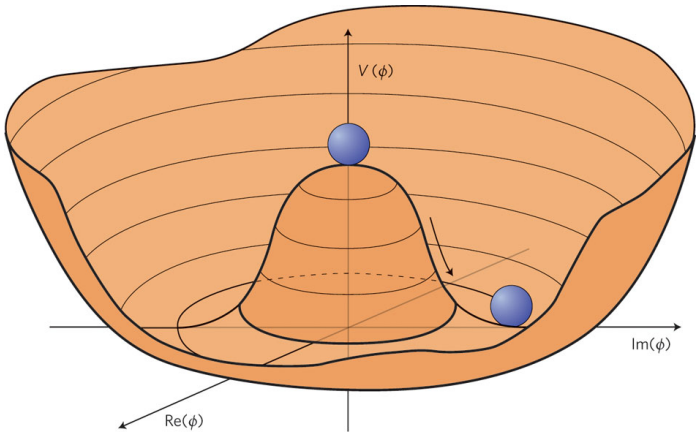

Figure 2.1: Illustration of the "Mexican hat potential."

represented by what is known as the "Mexican hat potential" (Figure 2.1). This potential has rotational symmetry, however, a lower energy state exists in the valley below. When a particle spontaneously "falls" into this valley, the local symmetry is broken and the particle obtains a non-zero vacuum expectation value (VEV). The result is a new massive spin-0 boson known as the Higgs, which was experimentally observed at the LHC in 2012 [2] [3]. In addition to imbuing the W and Z with mass, they Higgs can also be used to generate masses of fermions via Yukawa couplings. This phenomenon was experimentally confirmed by observing fermionic channels of Higgs decays.

Experiments at the LHC have been successful at confirming SM interactions and measuring their characteristics to a high precision. However, proton-proton collisions at the LHC are not the only source of high energy particle collisions. Cosmic events, such as supernovae and solar processes, can also generate high energy particles. Of particular importance to the stopped particle analysis are the cosmic rays that reach the earth's surface. Cosmic rays are high energy particles, typically protons and nuclei. These particles interact with the the earth's atmosphere, emitting additional

showers of particles that include pions. Some of these pion decays produce muons, which then bombard the earth's surface. These longer-lifetime particles with low dE/dx, can penetrate the atmosphere and even hundreds of meters of the earth's crust, allowing them to reach the LHC and its associated particle detectors. Since cosmic muons striking the detectors is a common occurrence and occur at a more or less constant rate, they have been central to commissioning and calibrating the experiments. They also are a primary source of background in the stopped particle analysis.

2.2 Supersymmetry

2.2.1 Limits of the Standard Model

The confirmation of the Standard Model has been a significant triumph in modern physics, but there remain several theoretical shortcomings of the Standard Model. The SM provides no explanation of dark matter or dark energy and thus only accounts for about 4% of the observed material in the universe. Theorists have also been unsuccessful in integrating the gravitational force into the inherently quantum mechanical SM. Though not explicitly a failure of the Standard Model, the individual masses of the fermions and the Higgs boson cannot be theoretically calculated from the fundamental constants and can only be determined empirically. The most concerning dissonance between theory and observation for LHC physics is the divergence arising from the radiative corrections to the Higgs mass. In particular, loop interactions between the Higgs and the massive top quark, W, and Z bosons rapidly inflate the mass of the Higgs, suggesting a significant inadequacy of the Standard Model.

2.2.2 Introduction of SUSY

A popular solution to the limitations of the Standard Model is the inclusion of Supersymmetry (SUSY), which would arise from some form of symmetry breaking present in the Standard Model. SUSY proposes that for each SM particle, there is a symmetric particle with spin offset by 1/2, meaning every boson has a fermionic superpartner, and every fermion has a bosonic partner. These supersymmetric particles provide a natural mechanism to cancel the Higgs loop interactions that cause the mass to diverge when the SM is renormalized by providing complimentary, opposite-sign terms to the mass corrections via the supersymmetric top and the fermionic partners to the SM gauge bosons. However, in order to provide this cancellation, the supersymmetric partners must have masses close to their SM pairs. This provides a strong theoretical motivation to search for SUSY particles with masses below approximately 1 TeV. The LHC is an ideal environment to search for such particles as it's large center of mass collision energy can easily produce particles with masses up to a few TeV. The SUSY particle would decay in analogous ways to SM particles, also producing SM particles in the decay chain. With these constraints, the energies of the decay particles would be on the order of a TeV and are well-suited for observation by LHC detectors.

Many variants of SUSY also provide good candidates for dark matter by predicting massive, colorless, weakly interacting, electrically neutral particles known as neutralinos ($\tilde{\chi_0}$). The neutralino is often proposed to be the lightest SUSY particle (LSP). Assuming R-parity, i.e. the conservation of the number of SUSY particles in a decay chain, the LSP would be present at the tail of all SUSY decays. These particles could be observed indirectly as missing energy in SUSY interactions, much like the neutrino is in SM interactions. In the stopped particle search, we assume that the gluino($\tilde{g}$) and stop ($\tilde{t}$) decay to their SM partners and a neutralino. Since

the neutralino would go undetected and, we search for signatures of the gluon and top resulting from the decays of the $\tilde{g}$ and $\tilde{t}$.

2.2.3 Split Supersymmetry

One particular sub-theory of SUSY, called split-SUSY, predicts the existence of long-lived gluinos. Split-SUSY earned its name due to the large mass splitting between the gluino and squark [4]. The theory was developed by ignoring the problem of the divergent Higgs mass (in split-SUSY, the mass of the Higgs is assumed to be fine-tuned) and instead focusing on the other problems of the Standard Model such as the lack of a dark matter candidate, the stability of the proton, and the unification of the SM forces with gravity. By ignoring the divergent Higgs mass, split-SUSY sets no requirements on the SUSY breaking scale, and as such it is allowed to appear as high as the Planck scale where the four forces are naturally unified. A particular advantage to split-SUSY is that it explains the nature of the extremely small cosmological constant by suggesting that our universe represents just one of a multitude of possible universes, and ours happens to be one with the vacuum energy required for the small cosmological constant.

In the theory, the gluino is assumed to be much lighter than the family of squarks, which are allowed to have masses up to the SUSY breaking scale, but it is required to decay to a squark and quark pair. Because of this large mass splitting, the gluino decay is highly suppressed and it may have a lifetime anywhere from a few nanoseconds to the age of the universe. The gluino is expected to loosely bind to valence quarks into bound states referred to as R-hadrons as a means of preserving color-confinement and would interact strongly with the material in the detector. Unfortunately, these R-hadrons would be obscured in the mess of particles and jets produced in pp collisions and thus would be difficult to distinguish from Standard Model interactions.

This is the primary theoretical motivation for searching for R-hadrons in time windows well away from collisions. At LHC energies, gluino with a mass on the order of 1 TeV would be produced with a low enough kinetic energy that it could be slowed to a stop within the body of the CMS detector. Once stopped, the R-hadron would remain at rest within the detector for hours or even months before decaying. The observation of such decays would provide strong evidence of split-SUSY, and thus a finely-tuned universe.

Chapter 3
The LHC and CMS

3.1 LHC

To understand the mechanisms for producing heavy quasi-stable particles at the LHC, it is instructive to first discuss a little about the accelerator. The Large Hadron Collider (LHC) is a dual-ring superconducting collider based on the border between France and Switzerland. To minimize cosmic ray flux, the LHC is situation approximately 100 m underground. The LHC is a 27 km (17 mile) ring in which two counter-rotating proton beams are injected. In2012, the LHC was operating with a center-of-mass energy $\sqrt{s}$ =8 TeV (4 TeV per beam), and it is expected to reach its design energy of $\sqrt{s}$ =13 TeV in 2015. It is capable of colliding particles in a proton-proton (pp), proton-ion, and ion-ion configuration. The data used for the stopped particle search are all collected in proton-proton mode, and so the following description will focus on this mode.

Protons are accelerated and injected into the LHC in a four step process. Initially, the protons are sourced and accelerated to 25 MeV beams in the LINAC2. The beams are then injected into the Proton Synchrotron Booster (SPB) where they are accelerated to 1.4 GeV. After this, they enter the Super Proton Synchrotron (SPS) and are further boosted to 450 GeV. The proton beams are then finally injected into

the main rings of the LHC where they are, in 2012, accelerated to 4 TeV per beam. Each time the beams are injected is referred to as a fill. A fill lasts until both beams are dumped.

The beams collide at 4 points around the LHC, including inside the CMS detector. To steer the proton beams around the ring, there are 1232 dipole magnets, accompanied by 392 quadrupole magnets used to focus the beam. In 2012, the beams were structured into individual bunches of protons spaced 50 ns apart. Ultimately, the LHC was designed to steer beams with bunches spaced by 25 ns, a period which is referred to as one BX. Individual bunches are gathered into bunch trains, typically containing 144 bunches per train. In 2012, there were an average of 9 bunch trains in each beam. There is also an 3 μs abort gap in each beam, which is necessary in the event that the beams need to be "dumped" from the LHC rings. Dumping the proton beams requires switching on a special set of horizontal deflecting kickers that will drive the beams outside of the circulating rings into an absorber made of graphite.

The number of possible collisions per BX is described by the instantaneous luminosity, defined as:

$$\mathcal{L}_{\rangle\backslash\int\sqcup\dashv\backslash\sqcup\dashv\backslash\rceil\wr\sqcap\int} = \frac{N_1 N_2 f}{A_{eff}} \tag{3.1}$$

The number of protons per bunch are given by N_1 and N_2, f gives the frequency of collisions, and A_{eff} is effective transverse area of the collision region, or approximately the transverse beam cross-section (which explains why it is important that the transverse area is small). Integrating $\mathcal{L}_{\rangle\backslash\int\sqcup\dashv\backslash\sqcup\dashv\backslash\rceil\wr\sqcap\int}$ over time gives the total luminosity. Notice that the units of luminosity are proportional to $area^{-1}$. Luminosity is defined in this way to make it easy to determine the event rate, n, which is given

by

$$n = \sigma\mathcal{L} \tag{3.2}$$

where σ is the cross-section of that particular event. Cross-sections are frequently given in units of barns[1] so luminosity is often expressed in units of b^{-1}. To illustrate this, at design energy, the LHC should produce 300 fb^{-1} per year[2], so any event with a cross-section of about 1 fb will be observed approximately 300 times per year.

In 2012, we recorded a maximum instantaneous luminosity of $7.5\times10^{33}cm^{-2}s^{-1}$ and a total integrated luminosity of 23.3 fb^{-1}.

A full description of the LHC can be found here [5].

3.2 CMS

The CMS apparatus (Figure 3.1) is a general purpose detector built surrounding one of the interaction points at the LHC. It was designed with two goals in mind. The first is to search for the Higgs boson, which would provide proof of spontaneous symmetry breaking in the electroweak sector. The second is to look for evidence of physics beyond the Standard Model. A detailed description of CMS can be found in [6]. A summary of the relevant features is included here.

The CMS experiment uses a right-handed coordinate system, the origin of which is at the interaction point of the two proton beams. The x axis points toward the center of the LHC. The y axis points up (perpendicular to the LHC plane), and the z axis is directed along the counterclockwise-beam. The polar angle θ is measured from the positive z axis and the azimuthal angle ϕ is measured from the x axis in the x-y plane, thus p_T is computed from the x and y components. The angle θ is used to

[1] 1 barn = $10^{-24}cm^2$
[2] 1fb = 10^{-15} b

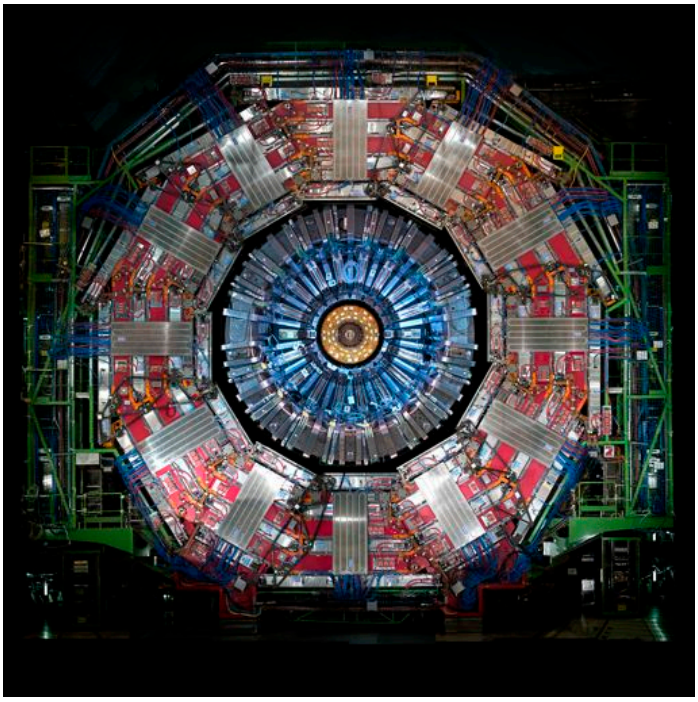

Figure 3.1: The CMS detector.

define pseudorapidity:

$$\eta = -ln\left(tan\frac{\theta}{2}\right) \tag{3.3}$$

The CMS apparatus has an overall length of 22 m, a diameter of 15 m, and weighs 14,000 tons. CMS contains a large cylindrical superconducting solenoid encasing the inner subdetectors, which generates a magnetic field of 3.8 T. Inside the solenoid are the silicon tracker, the electromagnetic calorimeter(ECAL) comprised of lead tungstate crystals, and a brass/scintillating hadronic calorimeter (HCAL). Outside of the solenoid are the muon detector systems. In the barrel region of the detector are drift tube (DT) chambers. In the two endcaps, cathode strip chambers (CSC) are used. In addition to these, resistive plate chambers (RPC) are spread throughout the barrel and endcap regions. A longitudinal view of the CMS detector is shown in

Figure 3.2.

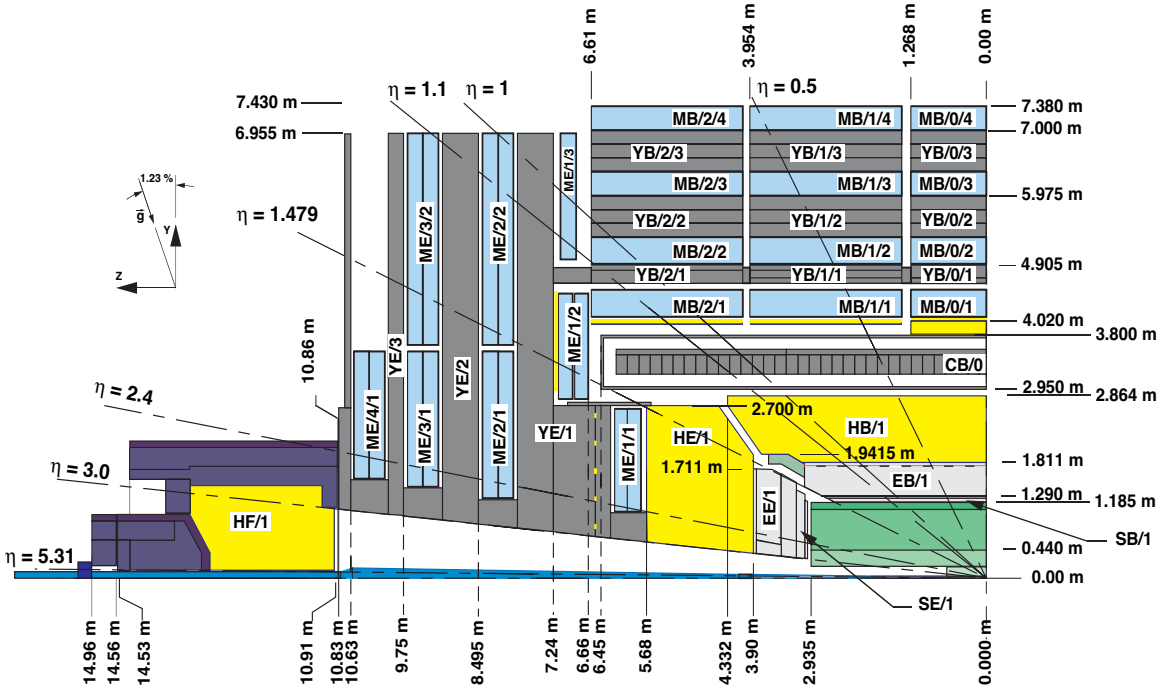

Figure 3.2: Longitudinal view of the CMS detector.

Because CMS was designed to be sensitive to such a wide range of physics, searches such as the stopped particle search can be developed even when they rely on characteristics of the detector that aren't typically considered. In particular, the HCAL is sensitive even to non-pointing hadronic decays, and the trigger system can fire on BXs away from pp collisions (both of which are necessary for the stopped particle search). The rest of this section will be devoted to describing the subdetectors from the innermost part of CMS outward. Particular focus will be given to the HCAL and muon system, which are central to the stopped particle analysis.

3.2.1 Tracker

The subdetector closest to the beam line is the silicon tracker. The tracker is designed to make precise measurements of the trajectories and momentum of charged particles immediately after they are emitted from collisions (neutral particles will pass through the tracker undetected). These measurements are also used to reconstruct the exact point of the pp collisions, called the vertex. Precisely determining the position of the vertex allows physicists to assign decay products to each of the multiple proton collisions that occur in high pile-up conditions. The tracker is also used to identify secondary decays from short-lived particles such as the b-quark.

The tracker is 5.8 m long and has an outer diameter of 2.6 m. The innermost region of the tracker is comprised of several layers of silicon pixel detectors starting at approximately 4 cm from the beam line. Outside the pixel layers are 10 layers of strip trackers. Each layer of the tracker is designed to be as thin as possible to minimize the effects on the particle's trajectory. The tracker exploits the electromagnetic interactions between charged particles and the silicon layers. When a charged particle passes through a tracker layer, it frees electrons in the silicon which are propelled by an electric field, inducing a current in the tracker electronics. There are a total of 1440 pixel and 15,148 strip modules in the tracker, providing coverage within the pseudorapidity range of $|\eta| < 2.5$. The tracker has a typical resolution of 1.5% in p_T and 10–90(45–150) μm in the transverse (longitudinal) impact parameter.

3.2.2 ECAL

The ECAL was designed to be compact enough to fit within the solenoid, while also being fast and radiation resistant, without losing the ability to make precise measurements. The barrel region has an inner radius of 1.3 m and extends out to

1.8 m. The endcaps begin at a distance of 3.9 m from the interaction point. It is a hermetic, homogenous structure composed of 61,200 lead tungstate ($PbWO_4$) crystals in the barrel and 7324 crystals divided between the two endcaps. These crystals were specially designed to be extremely dense and still transparent to visible light. An image of one $PbWO_4$ crystal is shown in Figure 3.3. To allow for fast readout between consecutive collisions, the crystals were designed so that 80% of light emissions occur within 25 ns. The ECAL provides pseudorapidity coverage of $|\eta| < 1.479$ in the barrel region (EB) and $1.479 < |\eta| < 3.0$ in the endcap regions (EE). The $PbWO_4$ crystals have a short radiation length of $\chi_0 = 0.89$ cm and are radiation hard up to 10 Mrad.

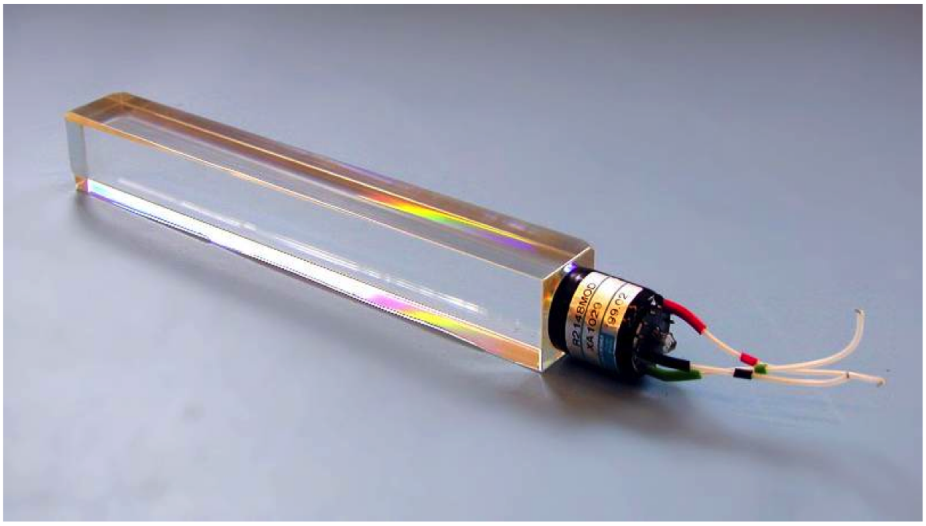

Figure 3.3: A lead tungstate ECAL crystal attached to the photodetector used to read out the light produced in the scintillating material.

When a particle passes through the ECAL, it interacts electromagnetically with the material of the crystals, resulting in heavily ionizing electromagnetic showers. Through a combination of pair-production and bremsstrahlung, particles will continue

to deposit energy as they traverse the ECAL. Energy deposited in the scintillating crystals results in the emission of blue-green scintillation light. This light is collected by photodetectors at the back surfaces of the crystals. Electrons and photons will come to a stop within the ECAL, depositing their full energy. In reconstruction, electrons and photons are distinguished by the presence (or absence) of tracks in the tracker. Muons and hadrons will leave energy deposits within the ECAL, but generally travel on to outer regions of the detector.

3.2.3 HCAL

If a particle escapes the ECAL, it then reaches the HCAL. As the name suggests, the HCAL's purpose is to halt hadrons and measure their position, energy, and arrival time. As a high-p_T particle passes through the HCAL, it hits alternating layers of dense metal absorbers and scintillation tiles. When it strikes the absorbers, the particle interacts strongly with the material, producing showers of secondary particles. A diagram demonstrating what a typical shower might look like is shown in Figure 3.4. When the particles in these showers deposit energy in the scintillation tiles, the tiles emit a blue-violet light that is read out via optical fibers to the external electronics. The intensity of this light is proportional to the energy deposited by the traversing particle. The HCAL is designed to maximize the number of interaction lengths that can be contained within the solenoid so as to completely halt hadronic particles before they may pass through the solenoid and strike the muon detectors. (As a form of ionizing radiation, muons can also leave small deposits in the HCAL as they pass through, but these deposits are significantly smaller than those produced by strongly interacting particles.)

The HCAL is a sampling calorimeter is composed of brass absorbers alternating with plastic scintillating tiles. Brass absorbers were chosen because they are

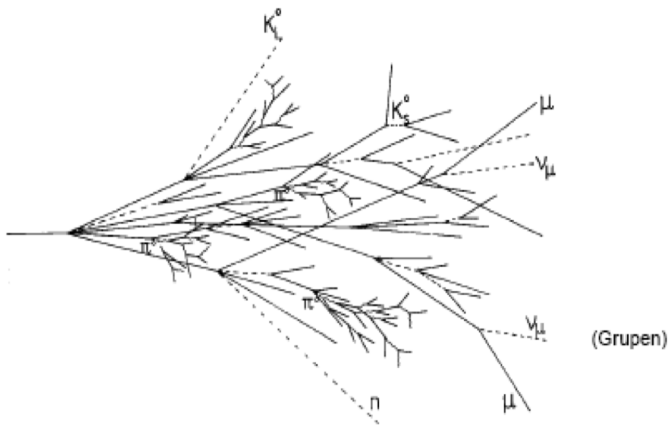

Figure 3.4: Diagram of the cascading interactions of a hadronic particle striking the brass absorber in the HCAL.

non-magnetic and have a short interaction length. The full depth of the HCAL exceeds nine interaction lengths, providing above 99% containment of incident hadronic showers. The tiles are made of plastic with embedded wavelength-shifting fibers that carry the light out to the hybrid photomultiplier tubes. The barrel region (HB) contains 2304 towers covering $|\eta| < 1.4$. The endcaps provide overlapping coverage from $1.3 < |\eta| < 3.0$. In the event that a very high energy jet traverses the HCAL without depositing its full energy, there is a single layer of absorber/scintillator outside the solenoid coil (HO).

The HB is of particular importance to the stopped particle search. Stopped particles are mostly likely to come to rest within the body of the HCAL, and we restrict our search to particles found in the barrel region. The HB is divided into two identical half-barrel sections, each with 18 "wedges". An image of an HCAL wedge is shown in Figure 3.5. An individual wedge is read out by a single read-out box (RBX). There are 4 hybrid photomultiplier tubes (HPD) in each RBX. A single HPD records signals from 18 calorimeter towers longitudinally arranged at constant ϕ. The HCAL

Figure 3.5: A single HCAL wedge in a test stand. The individual layers of brass absorbers are clearly visible.

cells map on to 5×5 ECAL crystal to form calorimeter towers projecting radially outwards from the interaction point. At larger values of $|\eta|$, the size of the towers increases and the matching ECAL arrays contain fewer crystals. Within each tower, the energy deposits in ECAL and HCAL cells are summed to define the calorimeter tower energies, subsequently used to provide the energies and directions of hadronic jets. The HCAL, when combined with the ECAL, measures jets with a resolution $\Delta E/E \approx 100\% \pm 5\%$ [7].

One of the three primary backgrounds of the stopped particle search is instrumental noise produced within the calorimeter. Occasionally, the HCAL produces anomalous signals that appear to be energy deposits, but are in fact the result of the subdetector malfunctioning. There are three varieties of HCAL noise [8]:

1. HPD noise

2. RBX noise

3. ion noise

HPD noise occurs when there is a misalignment between the electric field inside and HPD and the CMS solenoid, which lowers the flashover voltage of the HBD. This results in an avalanche of secondary electrons which can affect all 18 channels read out by the single HPD. This appears as a large energy deposit contained within a single value of ϕ. RBX noise is electronic noise within a single RBX that can affect up to all four HPDs read out through that RBX. Finally, ion noise looks like a large energy deposit in a single channel. It is caused by thermally emitted electrons that ionize the surrounding gas, which is then accelerated back into the cathode.

The vast majority of noise events are excluded by the centrally designed HCAL noise filter, which is applied to the data offline. This removes events in which at least 17 channels fire within a single HPD, or at least 10 channels fire in a single HPD with no activity in the rest of that RBX, or if a recorded noise pulse within a single RBX is spans more than two BX (some noise pulses tend to be more diffuse than energy deposits resulting from collision products). When coupled with additional information from the ECAL, the HCAL noise filter has an efficiency of >95% with a false identification rate of 0.4%. The stopped particle search has developed additional offline selection cuts to attempt to remove the final 5% and these are described in Section 5.5.3.

3.2.4 Muon Systems

The muon system is comprised of 3 separate gaseous detectors spread over the barrel and endcap regions, outside the solenoid coils. Because of the low dE/dx of the

muon, it can easily pass through the inner subdetectors without losing much energy (on the order of one GeV), necessitating additional subdetectors surrounding the detector. The design used in each region is determined by the muon rate, neutron-induced background rate, and the strength of the residual magnetic field. It covers the area $|\eta| < 2.4$. Figure 3.6 details the breakdown and geometry of the CMS muon system. The muon detectors measure the momentum of muons by collecting a series of position and timing measurements along the trajectory of the muon. Combined with knowledge of the topology of the magnetic field, the curvature of the path between these signals allows the calculation of the muon's momentum. All three subdetectors operate using the same principles. As a high-energy muon travels through the gas chambers, it knocks electrons off the atoms, which then congregate around positively charged wires within the chambers. The resulting avalanche of electrons are recorded. By measuring the width of both the pulse's position and timing distributions, the it can be reconstructed with great precision.

In the barrel region, where the muon flux is low, drift tube chambers are arranged over 5 wheels that can be separated to access the inner subdetectors. Each wheel is divided into twelve 30-degree sectors. A sector includes 4 measuring stations (MS) at increasing distance from the IP, alternating with layers of the return yoke. There is 1 DT chamber with twelve layers of drift cells in each MS, and each drift cell includes 8 layers of tubes parallel to the beam and 4 layers perpendicular. The measuring stations are staggered in ϕ to prevent gaps in coverage, ensuring a muon will hit at least three stations out of four, however because of the 5-wheel design, there are small gaps in coverage in z between wheels. Each drift cell reads out a time measurement corresponding to a muon hit, and the combination of time measurements provides a position measurement of the muon hit.

In the endcaps, where the radiation and muon flux is very large, cathode strip

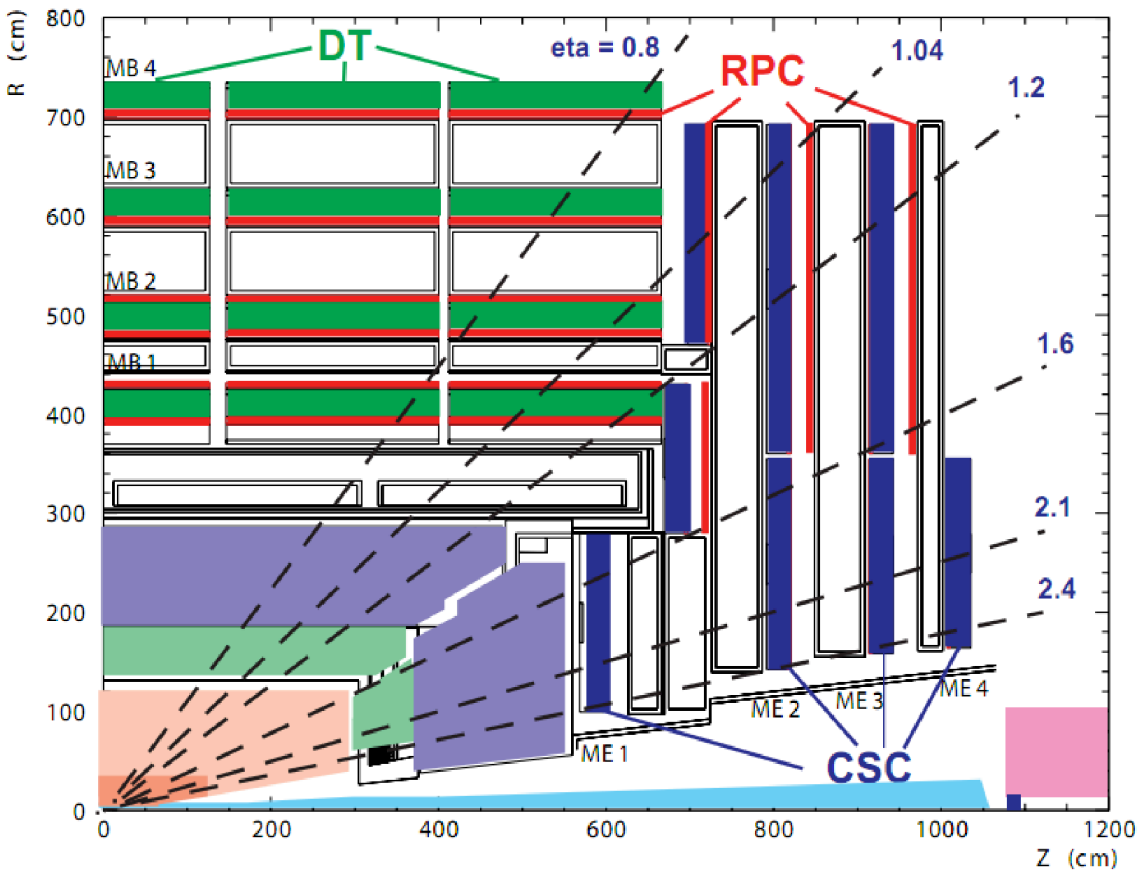

Figure 3.6: An r-z cross section of CMS with the muon system components labeled.

chambers are used. Each endcap has 4 disk-shaped muons stations (ME), which are divided azimuthally into 36 sectors. The outer three stations (ME2-4) are also divided radially into two rings, while ME1 is divided into 3 rings (the increased number of CSC chambers is required for the station closest to the IP due to the high flux). A single CSC chamber has 6 layers of cathode strips running radially from the beam line, and 6 layers of anode wires positioned concentrically at constant r. The anode wires provide the timing measurement for the muon hit, and the strips provide the position coordinates used to measure the muon's momentum.

The last system is the RPCs, parallel plate chambers that are fast and provide

high resolution for the timing of the hits, though they are not designed to provide good spacial resolution. Each DT chamber has 1-2 RPCs attached to it, thus a high-p_T muon traveling through the barrel can be recorded by up to 4 DT chambers and 6 RPCs. In the endcaps, RPCs are also interleaved between the CSC chambers.

Matching muons to tracks measured in the silicon tracker results in a relative transverse momentum resolution for muons with $20 < p_T < 100$ GeV of 1.3–2.0% in the barrel and better than 6% in the endcaps, The p_T resolution in the barrel is better than 10% for muons with p_T up to 1 TeV [9].

The stopped particle analysis, instead of using fully reconstructed muons, considers individually reconstructed hits within the muon systems. This increased degree of detail is important to make more aggressive cuts against possible background events. Hits recorded in multiple layers of a DT chamber are reconstructed as a DTSegment. These hits have a spatial resolution of 80–120 μm. In the CSCs, a combination of hits in multiple layers in a single chamber are combined into CSCSegments, which have a spacial resolution of 40–150 μm. One advantage to requiring hits in multiple layers of a single chamber is that the "direction" of the reconstructed CSCSegment can also be determined by calculating dx/dz and dy/dz over the individual hits in the chamber. RPCs, which are designed to provide excellent timing resolution, have a much lower spacial resolution of 0.8–1.2 cm. All three subsystems provide a timing resolution on the order of 3 ns. In addition to their precise spacial resolution, the CSCs and DTs are extremely efficient in recording muon hits (96%) and assigning them to the correct bunch crossing (99.5%) [10].

3.2.5 Particle Measurement

A drawing of a slice of CMS summarizing how different SM particles interact with the detector can be found in Fig 3.7.

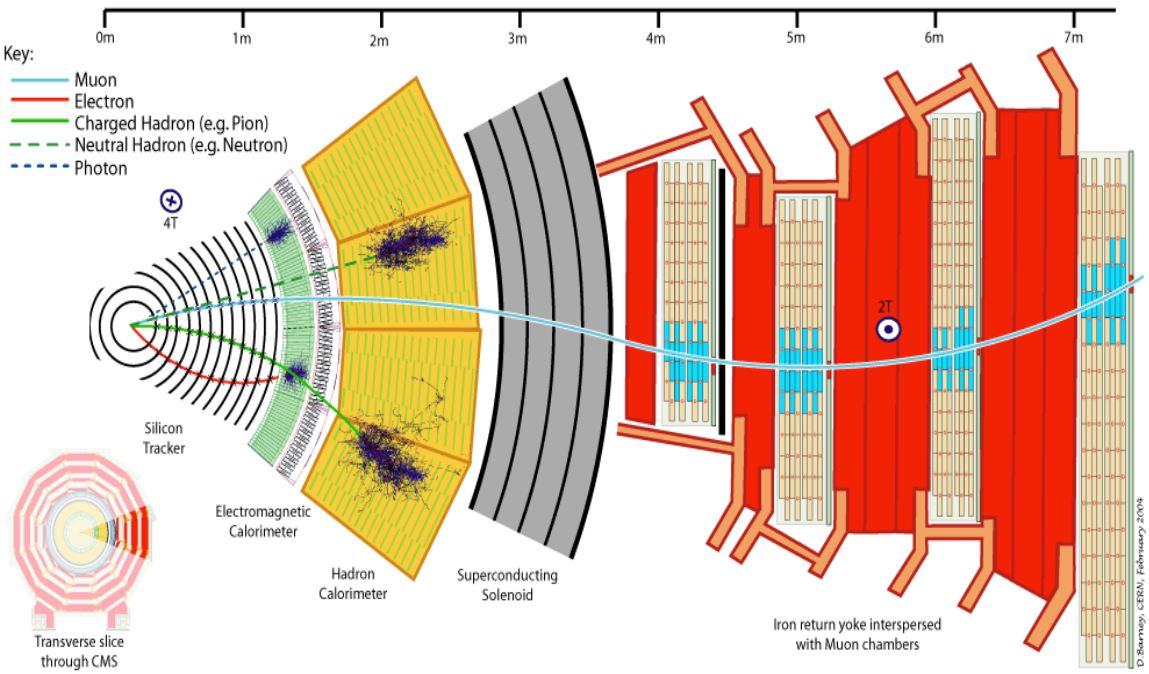

Figure 3.7: A look at the r-ϕ cross section of CMS including particle tracks as they traverse the detector.

Within CMS, photons deposit their full energy in the ECAL, escaping detection in the tracker due to the fact that they are electrically neutral. Electrons (and positrons) leave tracks in the tracker before losing all of their energy and stopping in the ECAL. With the help of the large magnetic field inside the CMS solenoid, the track of the electron is curved, allowing a precise measurement of its momentum. The direction of the curve determines if the particle is negatively or positively charged. A charged hadron, such as a π^+, leaves deposits in the tracker and ECAL before being captured by the HCAL. Its momentum is determined by the curved track in the tracker, and its energy is calculated by combining the energy deposited in the ECAL and HCAL. Neutral hadrons will only leave significant deposits in the HCAL, though comparatively small deposits are frequently left in the ECAL due $\pi^0 \to \gamma\gamma$ decays. Finally, muons will traverse the full length of the detector. As charged

particles, they will leave tracks in the tracker, and possibly small energy deposits in the ECAL and HCAL, before being measured by the muon systems. The majority of muons produced in pp collisions will continue out past the detector. The muon track bends less dramatically than the electron due to its larger momentum, but the curvature over the course of the full detector body is significant enough for its momentum to be successfully measured. Weakly interacting particles, such as the neutrino, will escape the CMS detector entirely without ever interacting with the detector material. Because energy is conserved in the transverse (x, y) plane, the calorimetry systems are used to measure the amount of missing transverse energy corresponding to a particular pp collision, which can often be assumed to be due to an escaped neutrino.

3.2.6 Trigger and Data Reconstruction

The LHC is designed to produce collisions at a rate of 40 MHz, or about 10^9 interactions per second. Data can not be read out at this rate and so and online trigger must quickly reduce the rate to 10^2 events per second. The trigger system in CMS is composed of two tiers. It starts a low-level trigger decision made by the front-end electronics on the calorimeters and muon systems. If any of these detect physics objects meeting a set of parameters, the subdetectors promote the trigger decision to the Level-1 (L1) detector-wide trigger system. By comparing reported trigger data from the subdetectors with a list of specially designed low-level trigger requirements, the L1 system determines if the event should then be fed to the High Level Trigger (HLT) system. The L1 trigger requirements are designed to produce a maximum rate of 100 kHz. Finally, the HLT accepts the event data and further decreases the number of events read out from 100 kHz to $\sim$100 Hz. The HLT is system is a high speed cluster of approximately 5000 computers. The rate reduction is performed by unpacking

the data and applying fast reconstruction algorithms to a given event. HLT trigger algorithms are applied to the reconstructed event to determine if it will be saved for further processing. The HLT can rely on one or more L1 trigger flags to do this, in addition to trigger algorithms used only at the HLT level. If an event passes the HLT requirements, it is then read out to disk for further, offline processing.

Offline, specially designed CMS software compiles raw data into well-defined physics objects such as jets, muons, and photons in a multi tier process. Initially, raw data is processed into candidate events at the Tier-0 computing server located at CERN. Tier-1 sites distributed globally additionally share the computing effort to produce refined event data with the final versions of each event's objects. Data is then distributed to over 100 Tier-2 and Tier-3 servers at labs and universities around the world, allowing individual analyses to access the data without overwhelming the T-0 and T-1 servers which require the full processing capability to reconstruct the events.

Chapter 4
Beam Halo Filter

In addition to developing the stopped particle analysis, I have been responsible for the CMS offline beam halo filter since the beginning of 2011. As beam halo is of particular importance to the search for stopped particles, the development of this software was relevant to my other work.

Beam-induced backgrounds can result in large missing transverse energy (MET) signatures unrelated to the collision event, or in the case of the stopped particle search, they can cause large energy deposits in the HCAL that can resemble our signal. Because many CMS analyses depend on an accurate calculation of MET to detect neutrinos or other neutral weakly-interacting particles, it is critical that anomalous signals caused by beam backgrounds be identified. Of particular concern are beam halo particles traveling parallel to the beam line that are produced with sufficient energy to traverse the length of the detector. These particles are generated when the proton bunches are focused and a "halo" of remaining un-focused protons continues to orbit away from the beamline, striking other parts of the LHC (such as the collimators) [11]. Some products of these collisions are either short-lived (such as pions and taus) and decay before reaching CMS. Others (such as neutrons and protons) may further interact with the LHC apparatus or the initial layers of the iron yoke within the CMS endcaps, stopping long before they can pass through the full

detector. Long-lived muons are mostly likely to reach CMS and because of the low rate at which they deposit energy in the material of CMS, they are the only particles that are likely to traverse the full length of the detector.

In an effort to identify events contaminated by these kinds of backgrounds, the BeamHaloID software package has been developed. The software filter relies exclusively on signals in the CSCs.

4.0.7 Beam Halo Signature

Beam halo is characterized by energetic muons traveling parallel to the beam approximately in-time with the proton bunches. A typical halo muon event is shown in Fig. 4.1. Though halo muons run parallel to the beamline, they are frequently observed as far as three meters from the beam, as shown in Fig. 4.2. Such particles can leave energy deposits in the calorimeters, either by emitting a photon via Bremsstrahlung, or by interacting directly with the scintillators, leaving anomalous deposits that do not correspond to a true energy deposit in the calorimeters. Because beam halo tends to travel in-time with the proton bunches, the outgoing leg of the halo is often indistinguishable from soft muons coming from collisions, but the incoming leg of the muon has a distinct timing signature that can be used to identify halo contamination.

4.0.8 Beam Halo Filter

The BeamHaloId package exploits information from the CSCs to identify events containing halo muons. CMS employs a L1 trigger based on CSC hits that tags potential halo events, which is used as an input to the filter. The CSCs geometry guarantees that it is nearly impossible for a halo muon to reach the calorimeters without leaving tracks in the CSCs. This is advantageous since beam halo is the most problematic

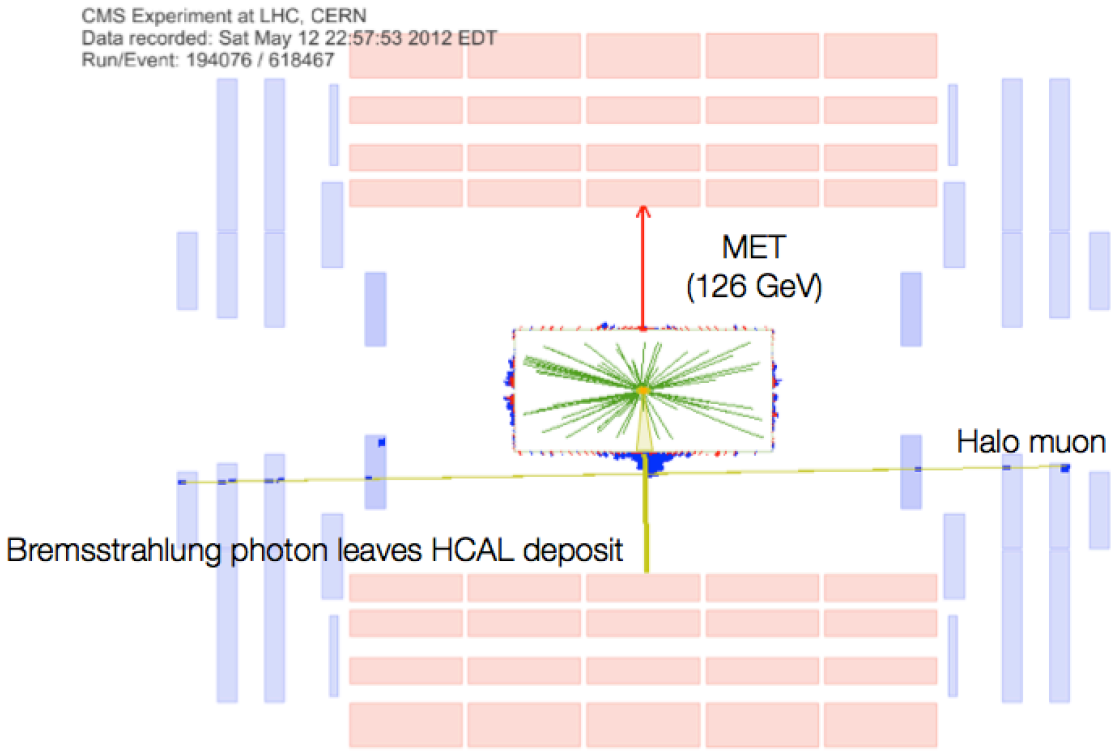

Figure 4.1: An example of a halo event showing the characteristic CSCSegments parallel to the beamline and a calorimeter deposit along the ϕ-axis, in this case in the HCAL. NOTE: the reconstructed vertex and tracker tracks (shown in green) are unrelated to the halo event, but are due to residual interactions between the detector and beam gas or noise in the tracker.

when measuring MET and MET-related quantities [12]. The excellent timing an spacial resolution of the CSCs also makes it possible to use the timing signatures and hit distributions of beam halo to tag contaminated events.

At the trigger level, there is a dedicated CSC-based L1 halo trigger that requires a minimum of two hits in at least two stations that are close in $\Delta\phi$, within 2°, with a maximum difference in $\Delta\eta$ of 0.2.

Beam halo identification also relies on reconstructed CSCSegments and muon tracks. There are two geometric measurements used to identify beam halo. The first

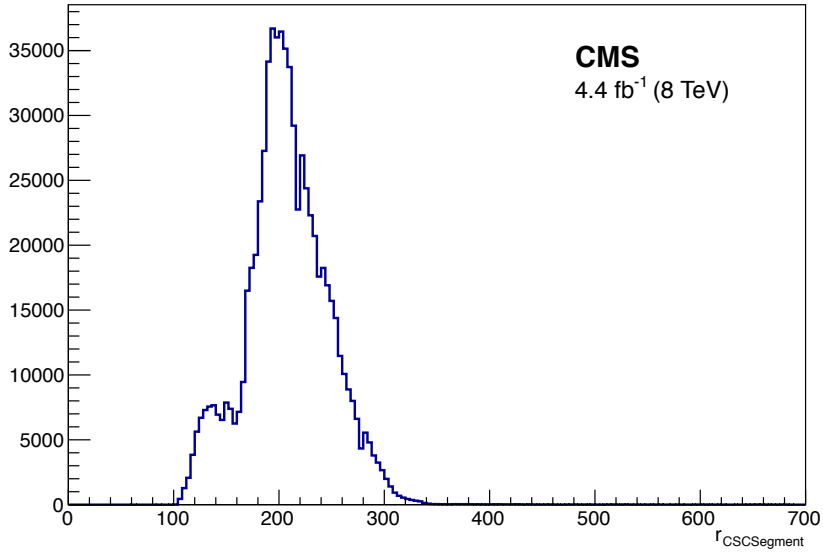

Figure 4.2: The radial distribution of CSCSegments associated with a tagged halo muon.

searches for halo-like tracks, requiring a reconstructed muon track approximately parallel to the beam that traverses both muon endcaps. There second operates at the CSCSegment level (for events in which the muon is not reconstructed) looking for multiple CSCSegments that fall within $\Delta r < 10.0$ cm and $\Delta\phi < 0.35$. In addition to these, CSCSegments are also required to be "flat," meaning the direction of the individual segments is parallel to the beamline. In the case that related segments are located in both endcaps, the event is definitively tagged halo, otherwise additional conditions must be met for the event to be tagged to decrease the fake tagging rate.

The unique timing signature of beam halo is a key component to identify events contaminated by beam halo. Because the incoming leg of the halo muon strikes the CSCs before the associated proton-proton collision occurs, the CSCRecHit times will be earlier than a collision muon. Thus events with a large number of early CSCRecHits ($t < -10$ ns) suggest the event contains a halo muon. However, as LHC bunch spacing

decreases, this signature alone can lead to false-positives due to the presence of muons from the previous collision. To keep the fake rate low, this input is combined with at least one other measurement to veto the event. The second timing-based input uses reconstructed halo muons. If there are enough hits in the CSCs for the muon to be reconstructed, we can look through the event's cosmic muon collection for signs of the incoming muon track. The reconstructed muon is likely beam halo if the outermost CSCSegment time is at least 10 ns earlier than the innermost CSCSegment time.

The beam halo filter combines the inputs above into a loose and a tight halo identification. The loose id requires the presence of only one positive input to veto the event, with the exception of the flat CSCSegments and the early RecHits - these must happen in tandem for the loose requirement, in order to decrease the fake rate. The tight id requires at least two positive inputs to veto, with the exception of finding flat CSCSegments (defined as $\Delta\theta < 0.7$ for a segment) at the same $r - \phi$ in both endcaps. This requirement alone is reliable enough to not need redundancy for a tight id.

4.0.9 Beam Halo Filter Efficiency in 2012

To determine the efficiency of the halo filter on data, I used a 2012 dataset produced with a MET trigger. By requiring events with $MET > 50$ GeV and at least one CSCSegment that is not a part of a reconstructed collision muon opposite in ϕ from the MET vector, we now have data that is mostly events containing beam halo. To estimate the number of remaining non-halo events, I plot $\Delta\phi$ between the CSCSegments and the MET vector. MET caused by beam halo will be at $\Delta\phi \approx \pi$. Using a simple side band subtraction where the background region is defined at $\Delta\phi < 3.0$, I estimate this sample to be about 86% pure halo. The distribution of $\Delta\phi$ between CSCSegments and the MET vector is shown in Fig.. 4.3 Taking into account the

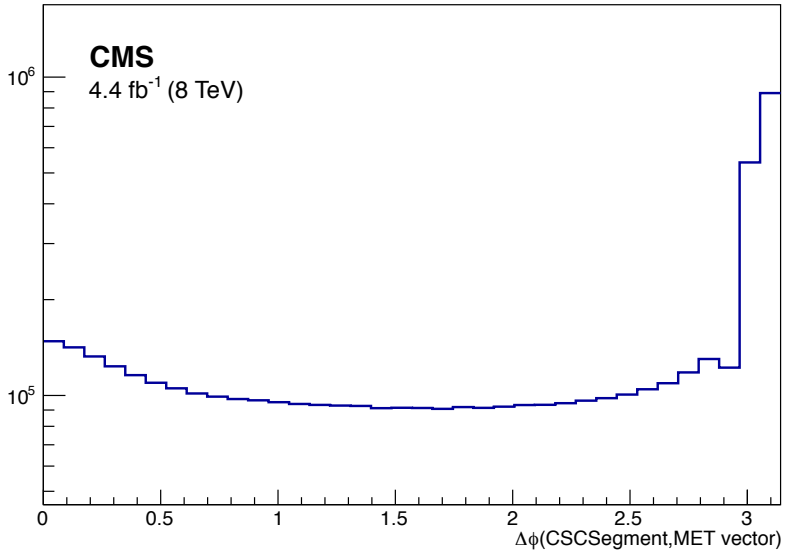

Figure 4.3: The distribution of the difference in ϕ between CSCSegments and the MET vector. The plot contains one entry per event. The CSCSegments due to halo are grouped above $\Delta\phi > 3.0$ and the background is presumed to be essentially in order to perform a sideband subtraction to estimate the non-halo contamination in the upper region.

contamination rate, the halo filter efficiencies are listed in Table 4.1. Events that escape the halo filter are primarily low-energy muons that fail to travel through more than one or two layers of the CSCs, and secondarily muons that do not meet the coincidence requirements of the L1 halo trigger.

Determining the fake rate is done by simply running the filter over a dataset known to contain little or no halo but at least one muon, so I used certified events in a data sample produced with a muon trigger that will only collect events with muons directed from the IP. The fake rates are listed in Table 4.2. The large fake rate using the loose tag is the result of flat, low-pT collision muons produced in the previous collision event, for instance from pion decays, or from calorimeter punch-through.

Halo Filter Algorithm	Tagging Efficiency
CSCLooseHaloId()	$99 \pm 3\%$
CSCTightHaloId()	$87 \pm 4\%$

Table 4.1: Tagging efficiency for the two CSC-based halo filter algorithms. Error includes both systematic and statistical uncertainty.

Halo Filter Algorithm	Fake Rate
CSCLooseHaloId()	$6 \pm 2\%$
CSCTightHaloId()	$0.4 \pm 1.0\%$

Table 4.2: The fake rate for the two CSC-based halo filter algorithms.

Chapter 5
The Search for Stopped Particles at CMS

5.1 Introduction

The stopped particle analysis is designed to search for long-lived particles produced in proton-proton collisions that halt within the detector and subsequently decay [13] [14]. In particular, we search for gluinos($\tilde{g}$) and supersymmetric top quarks($\tilde{t}$). This analysis assumes BR($\tilde{g} \rightarrow g\tilde{\chi_0}$)=100% and BR($\tilde{t} \rightarrow t\tilde{\chi_0}$)=100% (Figure 5.1). Only the SM daughter particle would be visible, meaning the decay signature will be a single jet deposit in the calorimeters. Because of the simplicity of the signal, the CMS collaboration designed a custom trigger that allows us to search in time windows during which there are no proton-proton collisions and the detector is generally quiet. This removes the complexity of sifting through Standard Model background events, especially QCD physics that would completely obscure the signal. Though the detector is generally quiet, there are several backgrounds that remain, namely beam halo, cosmic rays, and instrumental noise. Aggressive offline selection cuts are used to eliminate these backgrounds, as much is possible. Sophisticated techniques are then used to estimate flux of remaining background events that could escape the selection cuts. Using a combination of detailed data about the features of the LHC beams, the char-

acteristics of the observed events (namely timing and energy), and the background estimation, we employ a standard counting experiment to set limits on the cross sections of long-lived quasi-stable particles. In particular, the search focuses on the pair production of gluinos ($\tilde{g}$), and supersymmetric top quarks ($\tilde{t}$). While our selection cuts are very effective in vetoing background events, we also exploit the fact that our background flux falls off rapidly with with jet energy by increasing our minimum energy cut. While this is a powerful technique to restrict our background contamination, it comes at the expense of decreasing the region of phase space available to the search, thus we present results for a range of energy thresholds.

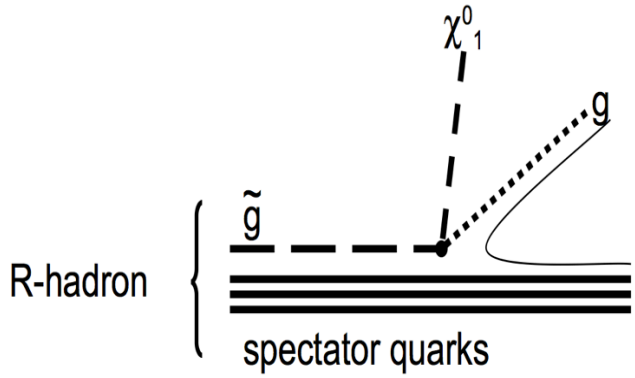

Figure 5.1: This analysis assumes BR($\tilde{g} \rightarrow g\tilde{\chi_0}$)=100%

In a complimentary search performed by ATLAS that also looks for stopped long-lived particles, the same techniques are employed, though they parameterize their limits differently. They also only place limits on the $\tilde{g}$, rather than including a search for the $\tilde{t}$. Their search includes 5.0 fb^{-1} from the 2011 7 TeV run and 22.9 fb^{-1} from the 2012 run at 8 TeV. Assuming a neutralino mass of 100 GeV and taking a

jet energy threshold of 300 GeV, their analysis excludes a gluino with lifetimes from 10 μs to 1000 s and $m_{\tilde{g}} < 857$ GeV [15]. Unlike the ATLAS analysis, our analysis parameterizes the limits based on the energy of the standard model daughter particle, leaving the neutralino mass unspecified. This is particularly important for the $\tilde{t}$ search where the exact mass of the neutralino can't be calculated when the top is off-shell. Our analysis covers the specific regions considered in the ATLAS search, but we are able to extend the phase space of our search by not limiting ourselves to particular neutralino masses.

5.2 Trigger

The CMS collaboration designed a custom trigger to record only events which are at least 25 'ns from a filled bunch (BX $\neq$ [-1,+1]) by using information provided by from the Beam Position and Timing (BPTX) monitors that are 175 m from CMS, along the beam axis on each side. The trigger also required a minimum HCAL energy deposit. For the control samples recorded in 2010, this threshold was set to 20 GeV. For the search samples recorded during 2012, this minimum energy threshold is 50 GeV. The trigger threshold had to be raised in 2012 to maintain a sufficiently low trigger rate. Finally, the trigger rejected any event which can be identified as beam halo at the hardware level by vetoing on a low-level beam halo trigger. Table 5.1 lists the filling schemes used in 2012 with the corresponding trigger livetime fractions.

5.3 Datasets

5.3.1 Control Samples

As a control sample, this analysis used 3.6 pb^{-1} of $\sqrt{s} = 7$ TeV pp collision data taken in the beginning of LHC operations in 2010, corresponding to 253 hours of trigger

Table 5.1: LHC filling schemes used for fills in the search dataset. The scheme names give the temporal spacing of bunches, to total number of bunches injected into the LHC, the number of colliding bunches at each of the 4 major detectors, and a description of the distribution of proton bunches within the beams.

Name	$N_{collision}$ / orbit	Livetime fraction
50ns_78b_72_0_48_36bpi3inj	72	94%
50ns_456b_447_0_431_72bpi12inj	447	68%
50ns_474b_465_0_452_72bpi12inj	465	71%
50ns_480b_471_0_461_72bpi12inj	471	71%
50ns_840b_807_0_816_108bpi12inj	807	49%
50ns_840b_801_0_804_108bpi13inj	801	49%
50ns_852b_807_0_816_108bpi13inj	807	48%
50ns_1374_1368_0_1262_144bpi12inj	1368	20%
50ns_1380b_1377_0_1274_144bpi12inj	1377	20%

livetime. The maximum instantaneous luminosity was 10^{28} cm^{-2}s^{-1} for this period, which is so low it is unlikely to produce signal. This control sample was only used to predict the instrumental background rates for the search. For details on how the 2010 data is used, see Section 5.6.2.

5.3.2 Search Samples

The search was performed over data taken between May and December 2012, during which 18.6 fb^{-1} of $\sqrt{s} = 8$ TeV data recorded by CMS was approved for analysis. This amounts to 281 hours of trigger livetime. Though the integrated luminosity for 2012 was significantly larger than that of 2010, the proton beams were more densely populated in 2012, and the amount of trigger time per-fill decreased substantially. 18.6 fb^{-1} represents 281 hours of trigger livetime. The maximum instantaneous luminosity achieved during this period was 7.5×10^{33}cm^{-2}s^{-1}.

There was a short period of data collection at the beginning of 2012 that could not

be used for the search due to a problem with the trigger configuration. Rather than vetoing on the beam halo trigger, we inadvertently rejected events using an arbitrary muon trigger. While this was unlikely to affect our search sample, the effects on the background rates could not be effectively modeled so this data period was excluded.

5.4 Monte Carlo

We generate signal Monte Carlo samples in three stages. First, we simulate $\sqrt{s} =$ 8 TeV proton-proton collisions using PYTHIA8 [16] [17], requiring the simulated collisions result in pair-produced gluinos, $\tilde{g}$, or supersymmetric top quarks, $\tilde{t}$. These particles are generated with long enough lifetimes that they can be treated as stable for the simulation. PYTHIA8 is also responsible for the subsequent hadronization. This first stage is performed for a range of gluino (stop) masses: 300 GeV $\leq m_{\tilde{g}} \leq$ 1500 GeV and 300 GeV $\leq m_{\tilde{t}} \leq$ 1000 GeV.

The resulting R-hadrons' passage through the detector is simulated with GEANT [18] where interactions between the R-hadrons and the detector material is simulated using the "cloud model" [19] [20] [21]. In this model, R-hadrons are treated as supersymmetric particles surrounded by loosely bound quarks. The cross section employed for these interactions is purely geometric, neglecting the mass of the R-hadron and instead treating it as a localized store of kinetic energy. R-hadrons are allowed to change flavor as they travel through matter via QCD interactions between the surrounding quarks and the nuclei of the detector material. If the R-hadron is charged, loss of energy in matter is due to combination of ionization and nuclear interactions. Neutral R-hadrons only interact strongly. While there is no means of experimentally verifying this particular model before such a particle is discovered, it is believed to be reasonable based on our current understanding interactions

between heavy, stable particles with matter, assuming R-parity is conserved for supersymmetry.

For R-hadrons with velocity $\beta \equiv v/c < 0.45$, it is possible they will stop within the body of the detector via nuclear interactions and (if the R-hadron is charged) ionization. For the particles that stopped, the position and flavor of the R-hadrons are recorded. This information is used as input for stage two of the simulation, as well as to estimate the stopping probability, $\epsilon_{stopping}$ (see Section 5.4.2).

In the second stage of simulation, we generate an R-hadron with the recorded flavor in stage one, translate it to the stopping position recorded, and decay it via a second GEANT step. This analysis assumes $\tilde{g} \rightarrow g\tilde{\chi_0}$ and $\tilde{t} \rightarrow t\tilde{\chi_0}$ with 100% probability. Stage 2 simulates the detector response to the R-hadron decay, including the trigger and data reconstruction. The trigger efficiency for masses ranging from 300 GeV $\leq m_{\tilde{g}} \leq$ 1500 and 300 GeV $\leq m_{\tilde{t}} \leq$ 1000 GeV can be seen in Figure 5.2. The second stage also provides an estimation of the reconstruction efficiency, ϵ_{reco} (see Section 5.5.5).

5.4.1 Toy Monte Carlo

The third stage of simulation is a toy Monte Carlo used to estimate the effectively luminosity (L_{eff}) (i.e. the amount of data taken that could produce particles that would decay when the detector is on and no collisions occur) for a given lifetime hypothesis. It is calculated with a statistical sampling technique applied to the full run period. Data is divided into 23 s periods called "lumi sections" (LS). CMS records the integrated luminosity collected in each LS. For each LS the following sampling procedure is carried out 1000 times: a random collision and a random, orbit within the LS is chosen. A specific decay time t is randomly generated from the distribution $e^{-t/\tau}$ where τ is the chosen lifetime hypothesis. If a particle produced at the chosen

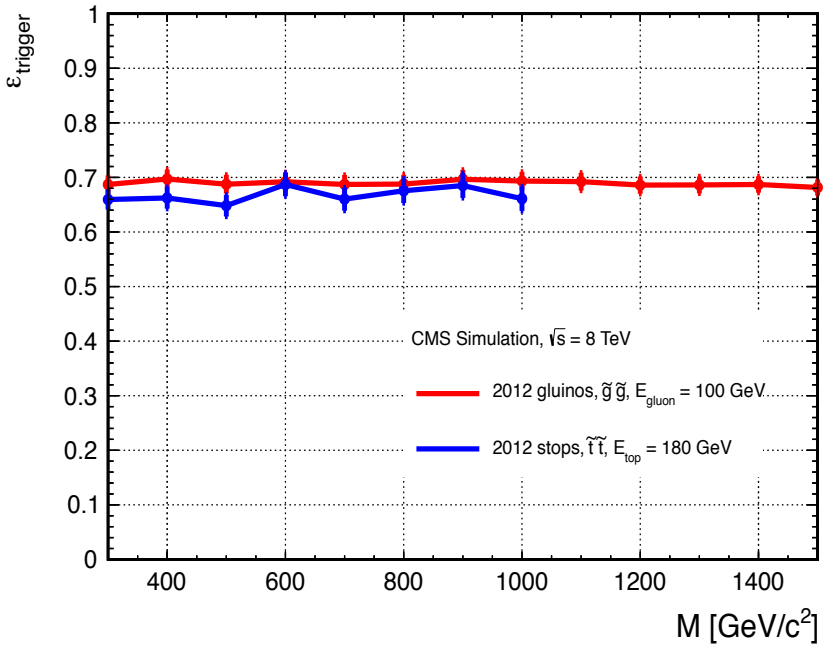

Figure 5.2: Trigger efficiency for $\tilde{g}$ and $\tilde{t}$ R-hadrons that stopped in EB or HB as a function of produced particle mass

collision BX and orbit decays with lifetime t during a period in which CMS is sensitive, the counter is incremented. After 1000 samples, we take the number of counted events divided by 1000 and multiply it by the recorded luminosity of that LS. The result is L_{eff} for that LS. This is performed for each LS and summed to find the total L_{eff} for the full dataset for a given lifetime hypothesis.

5.4.2 Stopping Efficiency

The probability of an R-hadron to stop within the instrumented regions of the detector is measured using Stage 1 Monte Carlo. The R-hadrons tend to stop in the densest regions of the detector. In particular, we consider R-hadrons that stop in the barrel regions of the ECAL (EB) and HCAL (HB) since these are the regions in which we are most likely to observe the subsequent jet-like energy deposits from the R-hadron's

decay. The R-hadrons also frequently stop within the iron yokes interleaved with the muon detector system, but it is unlikely that we would observe the corresponding decay due to our trigger requirements and the lack of appropriate instrumentation in these regions.

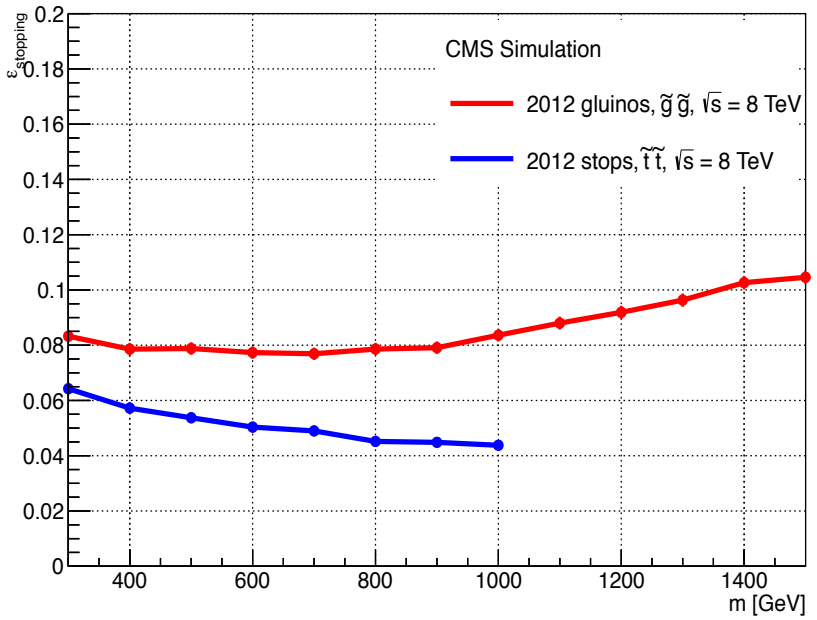

Figure 5.3: Stopping probability for $\tilde{g}$ and $\tilde{t}$ R-hadrons as a function of produced particle mass for both the 2011 and 2012 Monte Carlo samples.

Restricting our selected events to those which come to rest within EB and HB, Figure 5.3 shows $\epsilon_{stopping}$ as a function of $m_{\tilde{g}}$ and $m_{\tilde{t}}$ for 2012. We found in simulation that approximately 10% of the R-hadrons produced come to rest within the cavern walls, well away from the instrumented regions of the detector. We estimate only 0.02% of cavern-stopped particles leave a significant deposit in the HCAL and pass our selection cuts and so these events are excluded from our calculations of $\epsilon_{stopping}$.

5.5 Event Selection

Event selection is performed using offline cuts to remove our primary backgrounds: halo muons, cosmic muons, and instrumental noise; as well as secondary backgrounds: out of time pp collisions and beam gas.

Though non-collision BXs have such a low proton occupancy that they do not register as full by the BPTXs, there are still approximately 10^{10} protons per "empty" bunch. These bunches are not well-focused, but occasionally they do result in a collision. To remove these events from the search sample, we reject any event with a reconstructed vertex.

To account for fluctuations around the trigger threshold and the trigger turn-on curve, we reject any events with a reconstructed jet energy less than 70 GeV. This cut is increased in the higher threshold analysis described in Section 5.8.3.

5.5.1 Beam Halo Veto

Beam halo muons are one of the primary backgrounds contaminating our search sample. As discussed in Chapter 4, halo muons are produced when the proton beams are focused and so-called "halo" protons collide with the LHC apparatus, emitting a shower of particles. In almost all cases, muons are the only particles with a low enough dE/dx to traverse the full CMS detector. As these muons travel through the denser regions of CMS, they can emit a photon via Bremsstrahlung that strikes the calorimeters and can be reconstructed with a large enough energy to pass both our trigger and offline jet energy cut. We remove these events by vetoing any event in which there are recorded hits within the cathode strip chambers (CSCs) of the muon detector. The aggressiveness of the veto is necessary to exclude any possible halo event, which may register only 1–2 hits in the CSCs if the muon happens to pass

through a dead channel or strikes at a low angle.

5.5.2 Cosmic Muon Veto

Cosmic rays incident on the CMS detector are also a large source of background. Similar to the halo background, cosmic muons may emit a photon via Bremsstrahlung that strikes the calorimeters, leaving a large energy deposit. To remove such events, we consider the distribution of reconstructed hits within the barrel muon system. Compared to our expected signal, there are key differences with cosmic muons that can be exploited. It is possible that heavy R-hadrons' decay products can have enough energy to "punch-through" the outer region of the calorimeters and the first layers of the iron yoke of the solenoid, leaving energy deposits in the DT and RPC subdetectors. The challenge is to separate true cosmic muon events from the punch-through signal events. See Figure 5.4.

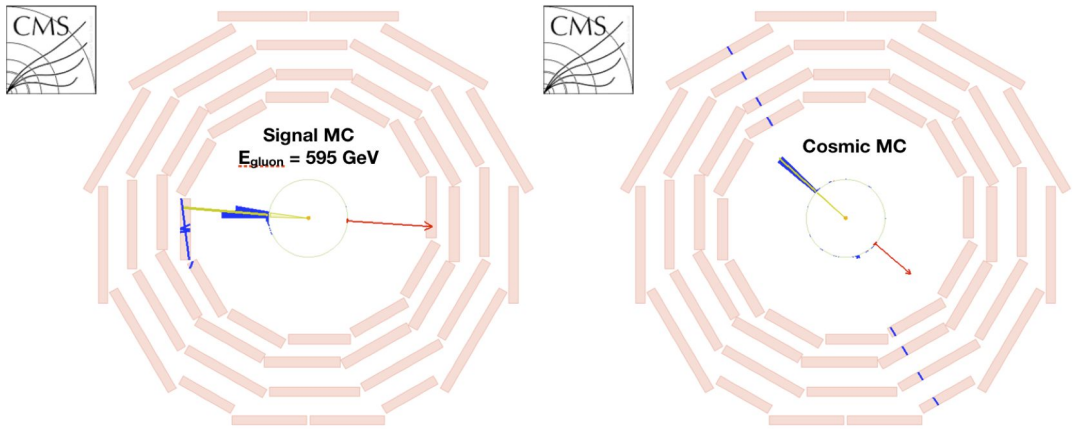

Figure 5.4: Event displays for signal MC with $E_{gluon} = 595$ GeV (left) and cosmic MC (right). Due to the punch-thru in the signal event, it would have been vetoed using a simple cut excluding evens with any activity in the barrel region of the muon systems.

This phenomenon in energetic R-hadron decays is distinguished from cosmic muons by considering the distribution of reconstructed hits. We expect punch-thru from signal to be concentrated in the innermost layers of the barrel muon system, whereas cosmic muons should leave hits in all layers. Punch-thru should also be very closely aligned in ϕ with the leading jet. This is true of cosmic muons as well, but we will only observe muon activity opposite the leading jet for a cosmic muon. Finally, muon hits will only be recorded on both sides of the detector (in ϕ) if the event is a cosmic ray. Using these characteristics, the offline cosmic cut was designed to reduce the energy dependence in the reconstruction efficiency while still maintaining a minimal cosmic veto inefficiency. It was determined that the following combination of cuts achieved both goals:

1. $\Delta\phi(DTSegment_i, DTSegment_j) > 2.0$
2. $\Delta\phi(DTSegment_i, jet) > 1.0$
3. $N_{looseOppositeRPCpairs} \geq 2$
4. $N_{tightOppositeRPCpairs} \geq 1$
5. At least 1 DT segment with $R > 560cm$
6. At least 2 RPC segments with $R > 560cm$

where a DTSegment is a reconstructed hit in a single layer of the Drift Tubes and an RPCHit is a reconstructed hit in a single RPC layer, i and j are indices of the DTSegments and RPCHits in the event, $N_{looseOppositeRPCpairs}$ is defined as the number of RPC pairs in which the two RPC hits are separated by at least $\phi > \frac{\pi}{2}$. $N_{tightOppositeRPCpairs}$ requires they be separated by $\phi > 3.0$, or almost exactly opposite one another.

Figure 5.5 shows comparisons between cosmic MC events and high energy signal MC events for the related values. In the top two plots, we show the difference in ϕ between any two DTSegments and RPCHits. Particularly for the DTSegments, the difference in ϕ is most likely to be less than $\pi/2$ for signal events, while cosmic events are more likely to have hits on both sides of the detector as the cosmic muon passes through the full body. The first plot on the bottom row shows the difference in ϕ between any DTSegment in the event and the leading jet. For signal, we again expect to see the DTSegments clustered near the ϕ-position of the jet as the muon hits are typically the result of punch-thru, while $\Delta\phi$ is more evenly distributed for cosmic events. The final two plots demonstrate that hits in the outer two layers of the barrel muon system are rare for signal events while they are quite common for cosmics. The $\Delta\phi$ plots are made per-segment rather than per-event because we were most interested in seeing the full distribution of muon hits for each event. They provide a good depiction of the differences between muon hits in cosmic and signal MC, allowing us to carefully determine cuts on the topology of muon hits to focus on cosmic events.

5.5.3 Instrumental Noise Veto

The final major source of backgrounds stems from instrumental noise in the calorimetry system, primarily within the Hadronic Calorimeter (HCAL). Faulty electronics in the HCAL give rise to events in which an errant spike in energy is recorded in the HCAL, unrelated to any physical interaction with particles produced in the detector. An in-depth discussion of HCAL noise is in Section 3.2.3. These events are incredibly rare, but they closely resemble our anticipated signal and must be carefully removed. We use a series of offline cuts developed by analyzing the well-defined timing and topology of these deposits to remove these events.

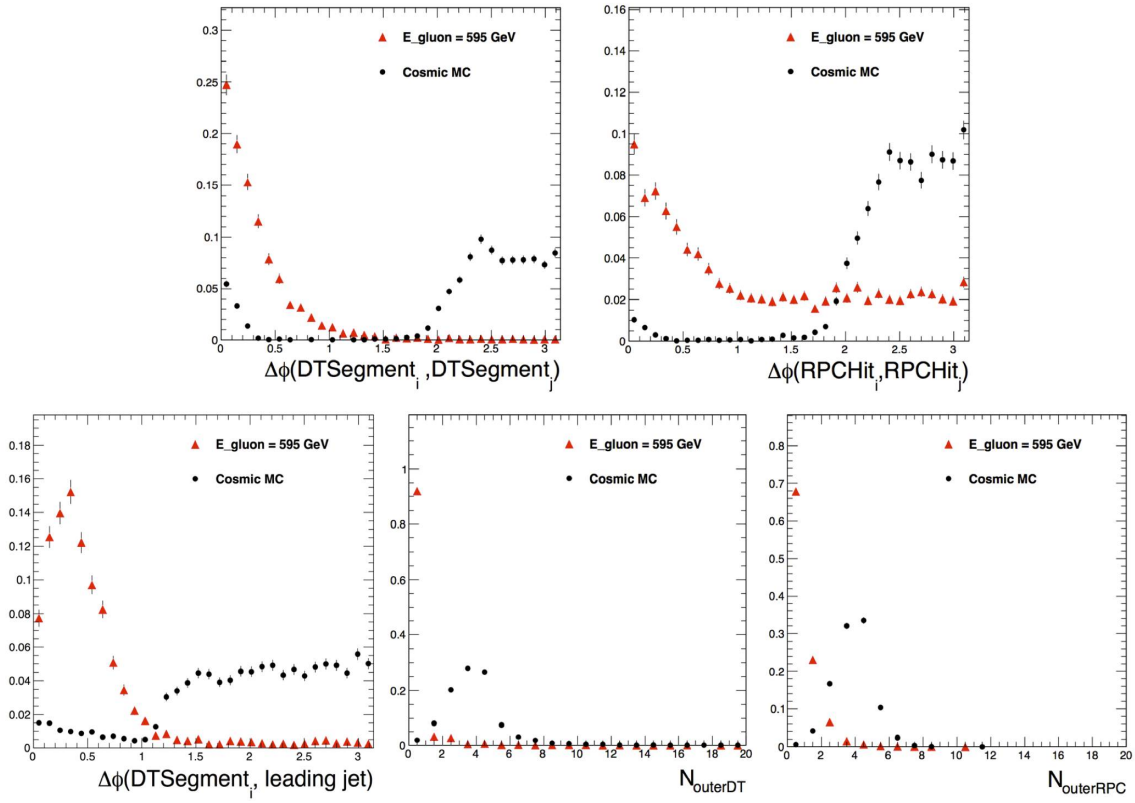

Figure 5.5: Comparison of barrel muon activity for cosmic Monte Carlo events and signal Monte Carlo with a gluon energy of 595 GeV

The primary cut we use is the standard CMS-recommended HCAL cleaning and noise rejection filter. In addition to the standard filter, we developed a set of our own custom cuts to further reduce noise contamination.

We remove events in which 90% of the energy of the leading jet is contained in more than 3 HCAL towers. A single hybrid photodiode (HPD) reads out 18 channels all corresponding to the same ϕ value. For a given jet, we sort the HCAL towers by energy, and count the number of leading towers at the same ϕ. If this value, n_{iphi}, is greater than 5, we reject the event. Finally, we compute the largest fraction of jet energy contained within a single strip of towers at constant phi, and we require that this value be less than 95%.

For the final four noise cuts, we consider the timing of the pulse in the HCAL. The physical pulse has some notable properties which can be used to distinguish it from the noise pulses. There is a clear peak bunch crossing, (BX_{peak}), significant energy in one bunch crossing before the peak ($BX_{peak} - 1$) and an exponential decay for several BXs following the peak. We have developed several powerful but highly correlated cuts based on these pulses. R_1 and R_2 characterize the exponential decay, R_{peak} characterizes the peak energy, and R_{outer} considers the energy of the pulse outside the 4 central BXs.

In previous iterations of this analysis, we also removed events that were 50 ns (BX ± 2) away from a proton bunch. In 2012, we examined the events with BX ± 2 in an effort to further understand our backgrounds. Previously, it was believed that this BX range was dominated by halo events and was excluded to reduce the background. With the 2012 dataset, we discovered that nearly all of the events showed no muon activity but had a single jet, often with substantial ECAL and HCAL activity, and always at approximately $\phi \approx -1.85$. The presence of ECAL activity suggested such events were not simply HCAL noise. It was determined that these were half of a collision di-jet event. There is a defect in the RBX corresponding to HPDs 52-55 in which this RBX periodically unlatches from the LHC clock and fires 25-50ns early. The result is di-jet events being split across multiple BXs, leaving a single jet in our triggered BX (Figure 5.6). This single jet closely mimics our expected signal, and because it is a physical jet in an otherwise quiet detector, it passes all of our cuts.

5.5.4 Full Offline Selection Cuts

To summarize, these are the conditions under which an event would be vetoed in the 2012 analysis:

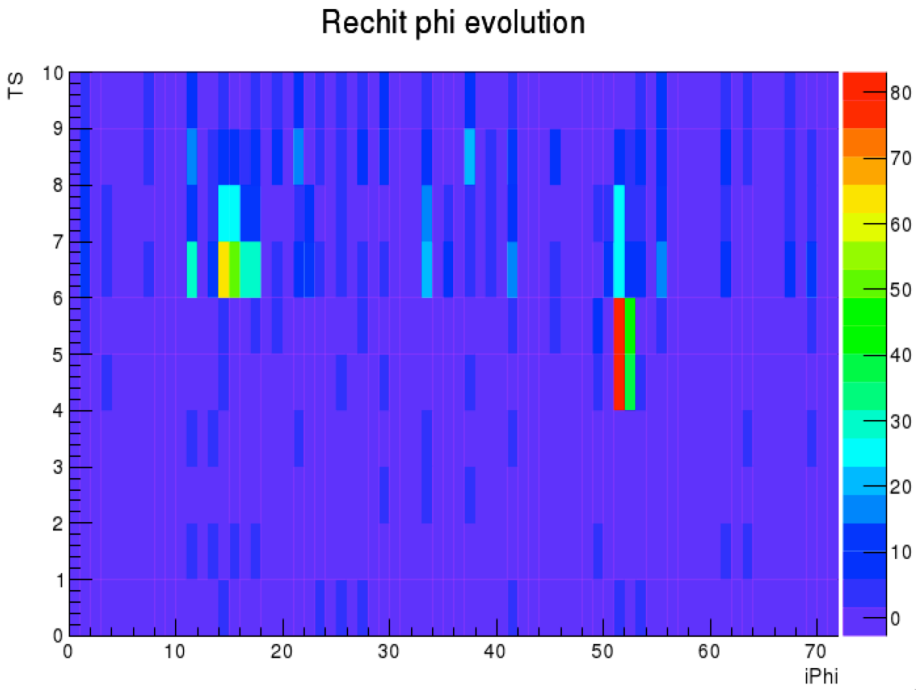

Figure 5.6: HPD number vs. recorded BX of jet deposit for a representative di-jet event. It can be seen here that one jet is read out 25-50 ns after the first jet.

1. Trigger requirement: Section 5.2

2. BX veto: bx of $\leq \pm 1$ with respect to a filled bunch

3. Vertex veto: event contains 1 or more reconstructed vertices

4. Halo veto: 1 or more reconstructed CSCSegments in the event

5. Cosmic veto: Section 5.5.2

6. HCAL noise veto: Section 5.5.3

7. $E_{jet} < 70GeV$: energy of the leading reconstructed jet is greater than 70 GeV

8. $n90_{jet} \leq 3$: 90% of the energy of the leading jet is contained in 3 or fewer HCAL towers

9. $nTowiPhi \geq 5$: the jet consists of 5 or more HCAL towers at the same iPhi

10. $E_{iphi}/E_{jet} \geq 0.95$: no more than 95% of the jet energy is deposited in towers at the same iPhi

11. $R_1 > 0.15$: $R_1 = E_{peak+1}/E_{peak}$

12. $0.3 < R_{peak} < 0.7$: $R_2 = E_{peak+2}/E_{peak+1}$

13. $R_{outer} < 0.3$: $R_{outer} = 1 - [E_{peak-1} + E_{peak} + E_{peak+1} + E_{peak+2}/E_{total}\ ]$

5.5.5 Reconstruction Efficiency

The signal efficiency is defined as the product of $\epsilon_{stopping}$ and ϵ_{RECO} (which includes the trigger efficiency). The method for determining the stopping efficiency is described in Section 5.4.2.

The reconstruction efficiency (ϵ_{RECO}) is defined as the number of signal events that pass all our selection criteria (including the trigger requirement) divided by the number of signal events that stop within the barrel region of the calorimeter. We assume BR($\tilde{g} \to g\tilde{\chi}^0$) = 100% and BR($\tilde{t} \to t\tilde{\chi}^0$) = 100%. ϵ_{RECO} depends principally on the energy of the visible daughter particle of the R-hadron decay, $E_{gluon}(E_{top})$.

We determine the minimum energy threshold for the SM decay products, E_{gluon} (E_{top}), to be where the turn on curve flattens out, i.e. when ϵ_{RECO} becomes approximately constant (Fig. 5.7). Above the minimum energy threshold of the visible decay products, $E_{gluon} > 120$ GeV ($E_{top} > 150$ GeV), $\epsilon_{RECO} \approx 45\%$ (32%) for $\tilde{g}$ ($\tilde{t}$) decays. In the cases where 150 GeV $< E_{top} < m_{top}$, the top is allowed to go off-shell.

In Figure 5.7, it is shown that above a gradual turn-on curve, ϵ_{RECO} is approximately constant for all values of $E_{gluon}(E_{top})$. We determine the minimum energy threshold for the SM decay products, E_{gluon} (E_{top}) for which the results are valid to

Table 5.2: Cumulative and N-1 counts for $m_{\tilde{g}} = 700$ GeV and $m_{\tilde{\chi}^0} = 536$ GeV, corresponding to $E_{gluon} = 145$ GeV. Given a total of 3841 events stopping the barrel calorimeters, $\epsilon_{RECO} = 45\%$.

Cut	Cumulative Count	Cumulative eff (%)	N-1 (%)
Stopped (EB+HB)	3841	100%	-
trigger	2820	73.4%	45.0%
BX veto	2820	73.4%	45.0%
Vertex veto	2820	73.4%	45.0%
Halo veto	2796	72.8%	45.1%
Cosmic veto	2482	64.6%	49.9%
HCAL noise veto	2221	57.7%	50.5%
$E_{jet} > 70$ GeV	1870	48.7%	52.6%
$n90_{jet} > 3$	1743	45.4%	48.1%
$nTowiPhi < 5$	1728	45.0%	45.3%
$E_{iphi}/E_{jet} < 0.95$	1727	45.0%	45.0%
$R_1 > 0.15$	1727	45.0%	45.0%
$0.1 < R_2 < 0.8$	1726	45.0%	45.0%
$0.3 < R_{peak} < 0.7$	1726	45.0%	45.0%
$R_{outer} < 0.3$	1726	45.0%	45.0%

be the point at which ϵ_{RECO} becomes constant. This is done for simplicity, at a small cost in signal sensitivity.

We fit the ϵ_{RECO} distribution to the error function $Erf(x)$ because it allows us to estimate that maximal value for ϵ_{RECO} and determine the minimum values of $E_{gluon}(E_{top})$.

$$Erf(x) = \frac{2}{\sqrt{\pi}} \int_0^x \mathrm{e}^{-t^2} \mathrm{d}t \tag{5.1}$$

using four parameters, A, B, C, and D:

$$\epsilon_{RECO}(E_{gluon}) = \mathrm{A}Erf(\mathrm{B}E_{gluon} - \mathrm{C}) + \mathrm{D} \tag{5.2}$$

Table 5.3: Cumulative and N-1 counts for $m_{\tilde{t}} = 400$ GeV and $m_{\tilde{\chi}^0} = 199$ GeV, corresponding to $E_{top} = 185$ GeV. Given a total of 2865 events stopping the barrel calorimeters, $\epsilon_{RECO} = 32\%$.

Cut	Cumulative	Cumulative eff (%)	N-1 (%)
Stopped (EB+HB)	2865	100%	-
trigger	1878	65.5%	32.1 %
BX veto	1878	65.5%	32.1 %
Vertex veto	1878	65.5%	32.1 %
Halo veto	1771	61.8%	33.1 %
Cosmic veto	1316	45.9%	40.4 %
HCAL noise veto	1163	40.6%	36.7%
$E_{jet} > 70$ GeV	968	33.8%	38.4 %
$n90_{jet} > 3$	935	32.6%	33.1%
$nTowiPhi < 5$	925	32.3%	32.5%
$E_{iphi}/E_{jet} < 0.95$	925	32.3%	32.1%
$R_1 > 0.15$	925	32.3%	32.1%
$0.1 < R_2 < 0.8$	921	32.1%	32.4%
$0.3 < R_{peak} < 0.7$	920	32.1%	32.1 %
$R_{outer} < 0.3$	920	32.1%	32.1 %

The efficiency on the plateau of this fit provides the central value of ϵ_{RECO}.

The systematic uncertainty is defined as:

$$\delta_{\epsilon_{RECO}} = \text{Maximum}(\frac{\text{Abs}(\epsilon_{RECO}(E_{gluon})_i - \epsilon_{RECO})}{\epsilon_{RECO}}) \tag{5.3}$$

where i indexes the E_{gluon} values on the plot.

For an energy threshold of 70 GeV, these values are $E_{gluon} > 120GeV$ and $E_{stop} > 150GeV$ with $\delta_{\epsilon_{RECO}} \approx 13\%$

5.5.6 Rates in Observed Data

In the 2010 control dataset, we observe a total of 2 events over a trigger livetime of 9.12×10^5 s which corresponds to a rate of $2.19 \pm 1.55(stat) \times 10^{-6}$ Hz. In the 2012

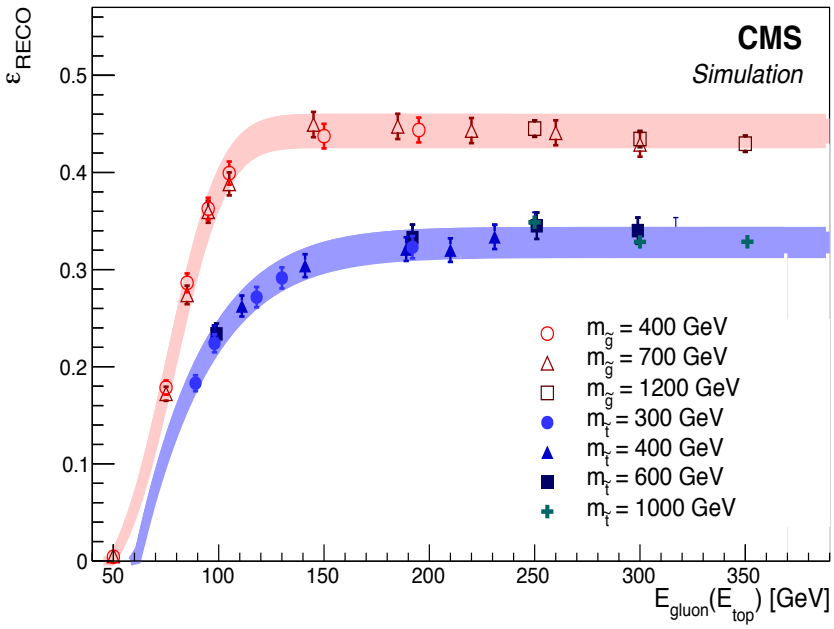

Figure 5.7: ϵ_{RECO} for $\tilde{g}$ and $\tilde{t}$ R-hadrons that stopped in EB or HB as a function of the energy of the SM daughter particle.

search dataset, we observe a total of 10 events over a livetime of 1.011×10^6 seconds, which corresponds to a rate of $9.89 \pm 3.13(stat) \times 10^{-6}$ Hz. The higher rate in 2012 is due to the presence of beam halo, which was not prevalent in 2010.

The cutflow tables for the 2012 search sample and the 2010 control sample can be seen in Table 5.4 and Table 5.5, respectively.

5.6 Backgrounds

Even with the sophistication of our offline selection cuts, there is a finite chance for background events to escape detection and be included in our group of observed events. In this section, the inefficiencies of the selection cuts for our primary backgrounds will be discussed.

Table 5.4: Cumulative and N-1 rates for all cuts, measured in the 2012 search dataset.

Cut	Cumulative Count	Cumulative eff (%)	N-1 (%)
trigger	3275614	100%	0.00031 %
BX veto	3262671	99.6%	0.00031 %
Vertex veto	3251175	99.3%	0.0030 %
Halo veto	1690878	51.6%	0.38 %
Cosmic veto	737122	22.5%	0.064 %
HCAL noise veto	217139	6.6%	0.048%
$E_{jet} > 70$ GeV	6119	0.19%	0.0027 %
$n90_{jet} > 3$	111	0.0034%	0.00079 %
$nTowiPhi < 5$	28	0.00085%	0.00040 %
$E_{iphi}/E_{jet} < 0.95$	12	0.00037%	0.00061 %
$R_1 > 0.15$	11	0.00036%	0.00031 %
$0.1 < R_2 < 0.8$	11	0.00036%	0.00031 %
$0.3 < R_{peak} < 0.7$	10	0.00031%	0.00036 %
$R_{outer} < 0.3$	10	0.00031%	0.00031 %

5.6.1 Cosmic Rays

The small inefficiency of the cosmic cut is assumed to be primarily geometric. For instance, nearly vertical cosmic muons can pass through CMS in or near the space between the wheels in the muon barrel. Since the cosmic muons pass through the detector a random times, it is also possible for only part of the cosmic muon's track to be recorded in a given event.

We produced a large sample of cosmic Monte Carlo to investigate the cosmic inefficiency. This sample is produced in GEANT by shooting simulated muons from the surface of the earth, down 100 m to the CMS detector.The inefficiency of the cosmic veto is defined as the the fraction of signal-like cosmic events that reach the detector, result in a trigger, but escape detection of the offline cosmic cut, divided by the total number of signal-like cosmic events. Out of 300 million simulated cosmic

Table 5.5: Cumulative and N-1 rates for all cuts, measured in the 2010 control dataset.

Cut	Cumulative Count	Cumulative eff (%)	N-1 (%)
trigger	2113645	100%	0.00009 %
BX veto	1887159	89.3%	0.0014 %
Vertex veto	1887152	89.3%	0.00009 %
Halo veto	1687355	79.8%	0.013 %
Cosmic veto	1388138	65.7%	0.057 %
HCAL noise veto	418799	19.8%	0.0035%
$E_{jet} > 70$ GeV	3794	18.0%	0.0032 %
$n90_{jet} > 3$	601	0.028%	0.0013 %
$nTowiPhi < 5$	5	0.00024%	0.00009 %
$E_{iphi}/E_{jet} < 0.95$	3	0.00014%	0.00009 %
$R_1 > 0.15$	3	0.00014%	0.00009 %
$0.1 < R_2 < 0.8$	3	0.00014%	0.00009 %
$0.3 < R_{peak} < 0.7$	2	0.00009%	0.00014 %
$R_{outer} < 0.3$	2	0.00009%	0.00009 %

events produced, approximately 115k events met the requirement of at least 15 GeV of missing E_t, which is used to ensure a minimal amount of energy deposited in the calorimetry system. Of those events, an additional 66k are rejected because they would be tagged as halo (leaving hits in the end cap muon system) or lack a reconstructed barrel jet. The remaining 49k simulated cosmic events resemble our signal closely enough to possibly contribute to our background.

Using these 49k signal-like simulated cosmic events, the cosmic veto inefficiency is then given by dividing the number of simulated cosmic events that escape the cosmic cut by the total total number of cosmic events.

In the process of validating the cosmic ray Monte Carlo, we determined that the distribution of simulated cosmic events does not accurately represent the data as well as we would like. In particular, cosmic data tends to have more RPCHits and fewer DTSegments than the simulation. In the comparison between simulation and data

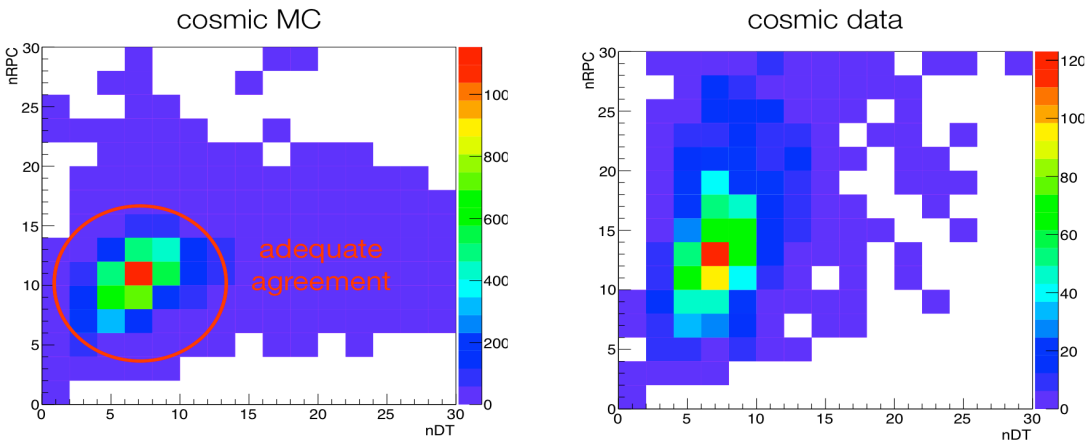

Figure 5.8: On closer inspection of the privately generated cosmic Monte Carlo, the distribution of DT and RPC activity must be normalized to the data due to differences in DT and RPC multiplicity.

shown in Figure 5.8, the plot on the left includes all of the 49k cosmic MC events that meet the minimum requirement of having a barrel jet and lacking CSC activity. On the right are data events passing all other section cuts excepting the cosmic veto. To further reduce the events to only those that are most likely cosmic muons, we also require the event to be tagged by the cosmic veto and to have twice as many outer DTSegments as inner ones.

To normalize the simulation to the data for the background estimate, which uses cosmic data, we bin the events in the number of hits in the DT and RPCs. Thus the inefficiency is calculated by dividing the histogram of cosmic events that escape the cosmic veto by the histogram of all 49k simulated cosmic events. The histograms used for this calculation are shown in Figure 5.9. Integrating the resulting histogram gives an rough estimate of the inefficiency at 0.5%.

The cosmic background estimate is calculated using this histogram of the inefficiency. The background estimate is calculated by multiplying the inefficiency histogram by a histogram of cosmic events selected from data. To ensure that the data

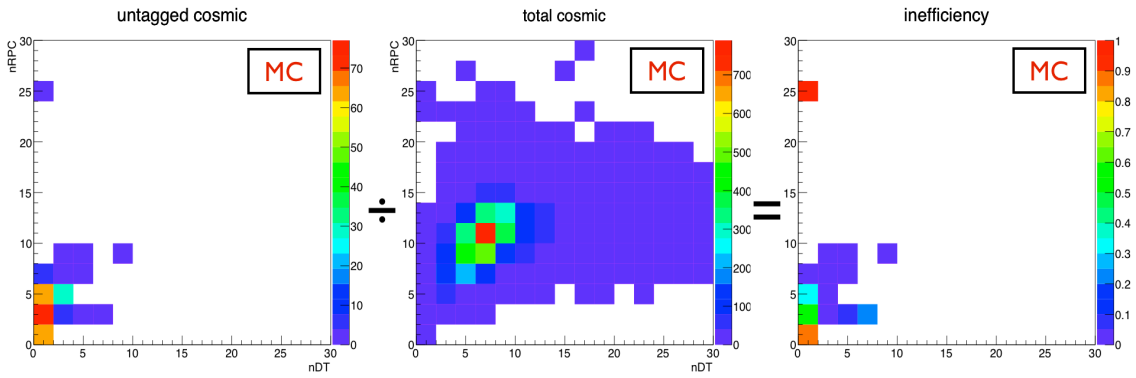

Figure 5.9: Cosmic inefficiency is calculated by dividing the number of untagged cosmic events by the total cosmic events. Due to differences between the simulation and data, we bin this in the number of DT and RPC hits so the result can be used to provide a cosmic background estimate.

includes only cosmic events, we require the events to pass all other selection cuts besides the cosmic veto. We additionally require that the event be tagged as cosmic by the veto and that there are more "outer" DT hits than "inner" ones. Due to the lower statistics in the data sample, we then fill in any empty bins by taking the average of the bins to the left and right. The difference between the original histogram and the interpolated histogram are shown in the first two plots of Figure 5.10.

To calculate the final cosmic background estimate, we multiply the inefficiency by the cosmic data events, binned in DT and RPC hits, and then integrate the final histogram to give the final background estimate of 5.2 ± 1.5 events. This estimate includes both statistical and systematic uncertainties due to the nature of the normalization. The systematic uncertainty of the inefficiency calculating is performed by adding 0.01 event, or about 1% of the total number of untagged events, to each empty bin in the untagged cosmic histogram and repeating the full calculation. This predicts and additional 1.0 background events. Combining these, we predict a cosmic background of 5.2 ± 2.5 events.

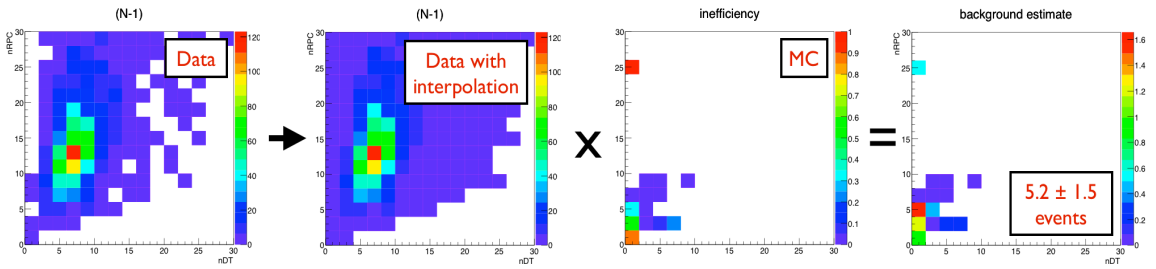

Figure 5.10: The estimate of the cosmic background is determined using cosmic MC, binned in N_{DT} and N_{RPC}, to compute the inefficiency and applying the result to the distribution of positively identified cosmic events passing all other selection cuts.

5.6.2 Instrumental Noise

We use the 2010 dataset to determine our noise background. During that time the luminosity of the beams was sufficiently low that we assume no signal events are present. Additionally, the noise rate should be approximately constant for all run periods given that no significant changes have been made to the HCAL structure (See Fig. 5.11 to compare the noise rates for the two eras). The low luminosity in 2010 also means that there should be practically zero halo events. The difference in rates observed between the two run periods is due to the large flux of beam halo in 2012. The only remaining observed events would then be cosmic rays or instrumental noise. The cosmic ray rate can be well determined using the method described in Section 5.6.1, but it is impossible to model the instrumental noise rate in simulation. To determine the central value of the noise estimate, we compare the number of expected cosmic ray events from the total number of selected events. In this case, only 2 events are observed with a cosmic background estimate of 4.8 ± 3.6 events. Because the cosmic background estimate exceeds the number of observed events, we assume a central value of 0 events for the noise estimate.

To calculate the statistical and systematic error of this method, we use the cosmic

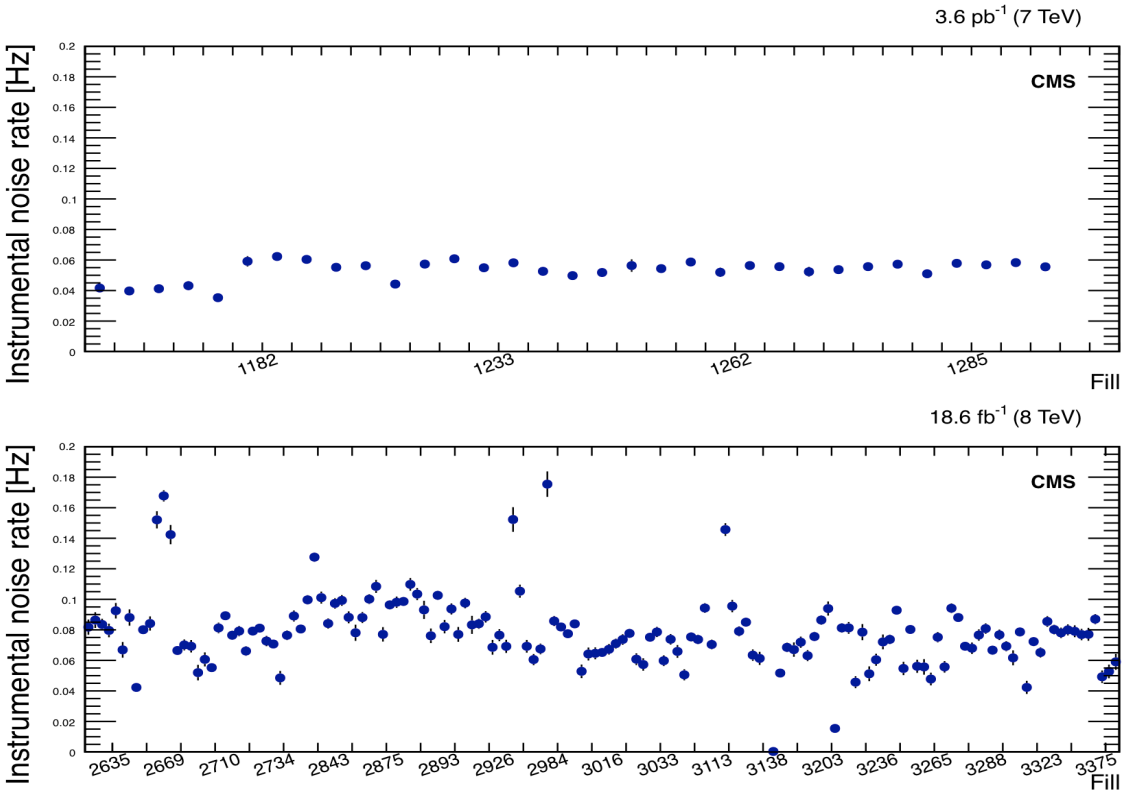

Figure 5.11: The noise rates for 2010 (top) and 2012 (bottom). In these plots, noise events are defined as events passing the cosmic, halo, and vertex veto. There is a greater variation in the 2012 noise rate due to the increased halo background, which can mimic noise if no CSC hits are present. This variation is small compared to the larger systematics due to low statistics in the number of selected noise events.

background estimate and the number of selected events in that era to perform a toy counting experiment. We can assume that the cosmic muon rate is constant in time and well-modeled by a Gaussian distribution centered at the background expectation. By convoluting the Gaussian with a Poisson distribution in which the parameter is the number of observed events in 2010, we can sample the likely number of cosmic events, which is treated as the background. A second sampling from a Poisson distribution in which the parameter the the number of observed events in 2010 provides the 68% CL limit of observed events. Over 1000 samples, the counting experiment predicts a limit

of 2.3 events at 68% CL, giving a noise estimate for the 2010 period of $0.0^{+2.3}_{-0.0}$ events. This estimate is then scaled by the 2012 livetime, resulting an expected $0.0^{+2.6}_{-0.0}$ noise events in the 2012 dataset.

5.6.3 Halo Muons

The halo background estimate employs a data-driven tag-and-probe method comparing the presence of incoming and outgoing "tracks" of the halo muon. We bin halo events in the (x, y) position of the reconstructed CSCSegment due to the fact that the (x, y) distribution of halo is well-understood. Halo activity is highly dependent on the distance from the beampipe, as well as the position in ϕ due to off momentum and magnetic rigidity distributions of the beams (Figure 5.12). With the high statistics in 2012, we are able to separate beam 1 and beam 2, so as to create isolated estimates for each by using the CSCSegment timing and z-position to determine the direction the muon was traveling when it struck the CSC chamber. Because of the physical properties of the LHC, there is significantly more halo present in beam 1. (Beam 2 typically has only $\sim 1\%$ of the beam halo present in beam 1).

The tag-and-probe analysis includes any event meeting these criteria:

1. Passes the signal trigger
2. Has at at least 1 reconstructed jet
3. Has reconstructed CSCSegments in at least 3 layers
4. Has at least 1 reconstructed CSCSegment within $\Delta\phi < 0.4$ of the leading jet

Plots showing distributions of the CSCSegment times are in Figures 5.13 and 5.14.

Ideally, a high energy halo muon will fully traverse the full length of the detector, providing both incoming and outgoing tracks. However, due to energy loss within the

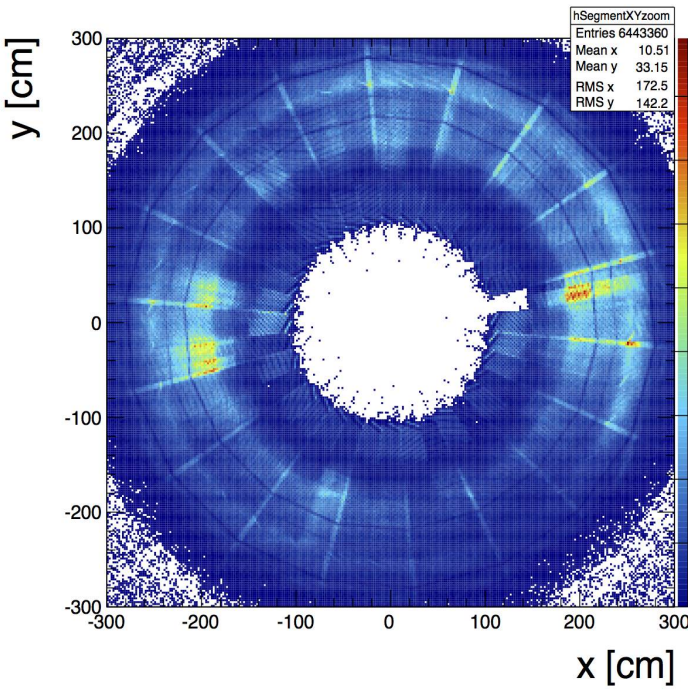

Figure 5.12: The (x, y) distribution of all CSCSegments passing our signal trigger.

detector, we may only see the incoming leg. Due to timing and trigger effects, only the outgoing leg may be recorded. Geometric inefficiencies can affect both incoming and outgoing legs. Based on on this information, each halo event is categorized based on which part of the halo muon "track" is recorded: incoming, outgoing, or both. Using the information on the direction of the muon, we further distinguish between beams 1 and 2.

Next, we calculate the average (x, y) position of every CSCSegment in the event and histogram the event according to it's category, binned in the average (x, y) of the whole event. The probability for a halo muon to traverse the detector without being detected is then $\frac{(IncomingOnly)\times(OutgoingOnly)}{(Both)\times(All)}$. We approximate "All" by the sum of the other 3 categories, which is sufficient due to the significantly smaller number of missed halo events. The histograms for beam 2 are binned more coarsely due to

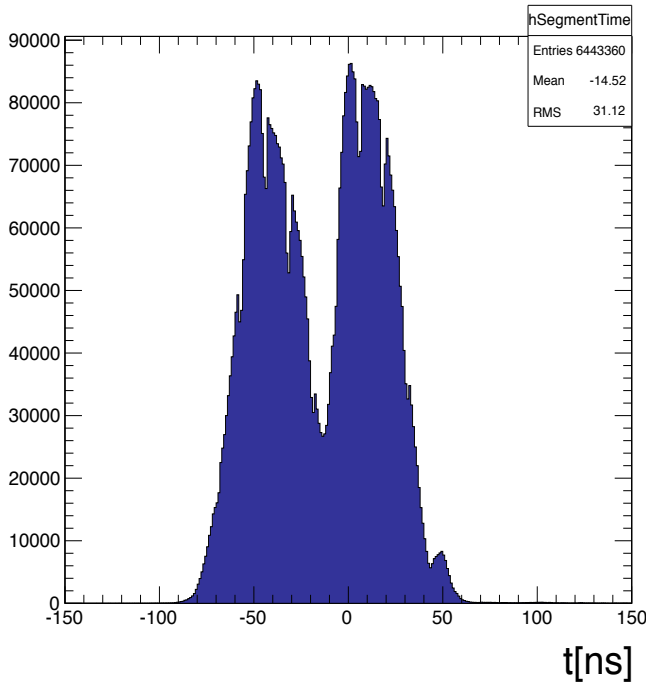

Figure 5.13: The recorded time of CSCSegments. t = 0 is the midpoint of a BX.

lower statistics. The resulting histogram is then multiplied by the (x, y) distribution of positively identified halo events passing all other selection cuts (see Figure 5.15). By integrating over the resultant, we get a background estimate of 8.0 ± 0.2 events.

In order to determine the systematic uncertainty of the way the events are binned, we repeated the same process, but this time binning in (r, ϕ). There is approximately a 3% difference between the methods, so the final estimate becomes $8.0 \pm 0.2(stat) \pm 0.2(sys)$.

5.7 Sources of Systematic Uncertainty

The search for stopped particles described here is, by design, minimally exposed to systematic uncertainties. The systematic uncertainty due to trigger efficiency is negligible since the offline jet energy cut ensures the data analyzed are well above

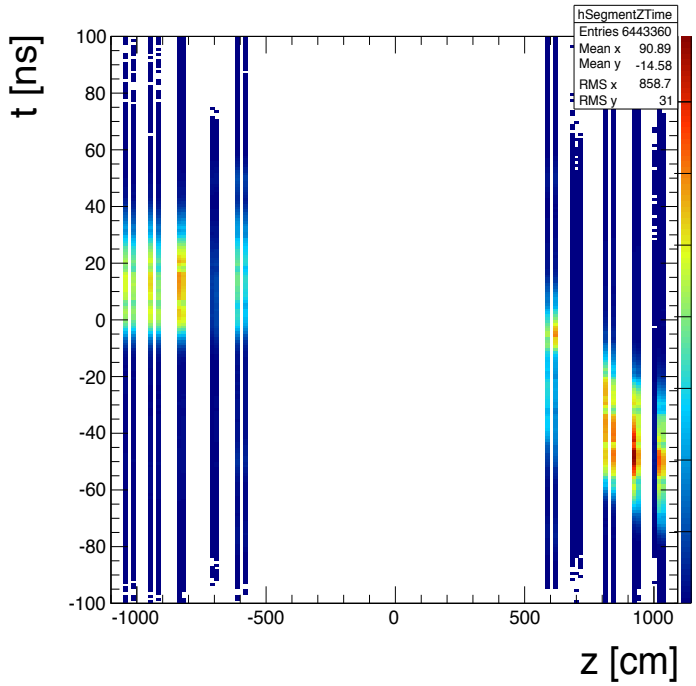

Figure 5.14: The $(z, time)$ distribution of all CSCSegments passing our signal trigger. This plot also shows that the majority of halo muons are traveling in the -z direction, which is the direction of beam 1.

the turn-on region. There is a 2.6% uncertainty on the luminosity, which is the standard value provided by the CMS collaboration. The small energy dependence in the signal efficiency described in Section 5.5.5 results in a 13% uncertainty on the RECO efficiency.

Accounting for the uncertainty in the Jet Energy Scale (JES) is a challenge for this analysis. Because the energy deposits resulting in reconstructed jets aren't like jets originating from the IP, they are not necessarily directed radially. All estimates of the JES uncertainty produced by the CMS collaboration make assumptions about the origin and direction of the jet, and so are inappropriate for this search.

In a period in 2008 during which CMS was collecting exclusively cosmic ray data due to the lack of beam in the LHC, the HCAL group performed a study using

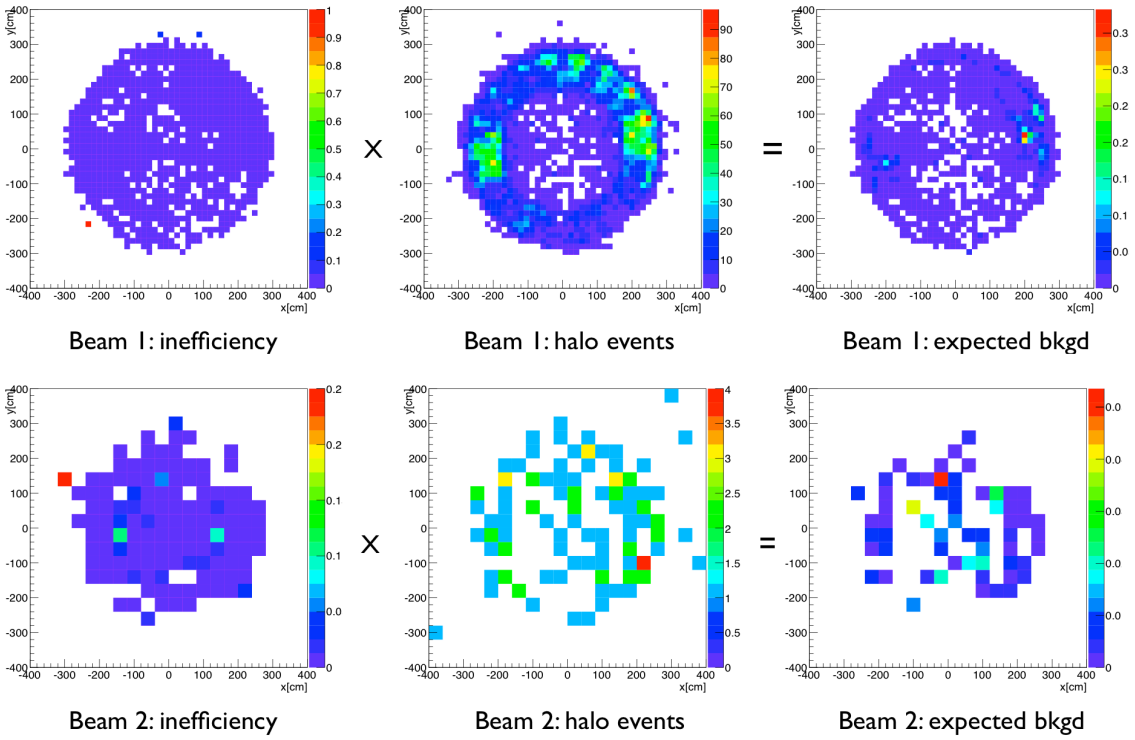

Figure 5.15: Distributions of the data-driven estimate of the halo veto inefficiency, the positively-identified halo events in the search sample, and the resulting estimate of the total halo background, separated by the corresponding beam.

cosmic rays to validate the absolute energy scale and the material descriptions in HB simulations in GEANT [22]. The advantage to this study is that the cosmic rays do not necessarily follow the path through the HCAL that a collision muon or jet would. This provides us information about how well the simulation models non-radial HCAL deposits. For ionizing events with muon $pT < 100$ GeV, the simulation and cosmic ray data agree to within 2%.

In addition to the this 2008 study, we also consulted an internal CMS note describing jet performance in the 2012 era based on dijet and Z+jet events [23]. While standard jet energy corrections are not applicable to this search (since all corrections assume jets originating at the IP), the studies on the absolute jet energy scale compar-

ing data and MC are considered. For jets at $\eta < 0.0$, the reported JES uncertainty is $\approx$ 1%, increasing up to $\approx$ 5% at $\eta < 2.8$. We use this range to determine the JES uncertainty for jets striking the HB at various angles of incidence. Because the scintillator tiles in the HB run parallel to the beam line, as the pseudorapidity of a collision jet increases, its angle of incidence to the tiles also increases. The maximum angle of incidence is achieved at the end of the HB ($\eta = 1.3$) where a collision jet would strike 60° from the normal. For the full range of $0.0 < \eta < 1.3$ ($60° > \theta > 0°$), the study shows a maximum JES uncertainty of $\approx$ 2%. Given this range of values, we are confidant that the appropriate JES uncertainty is $\leq$3%. This value is somewhat conservative compared to the HCAL study's results, we want account for any increase in uncertainty for decays at extreme angles not possible to observe with cosmic or di-jet events. With this uncertainty on the jet energy scale, we find the signal efficiency varies by about 2%.

Figure 5.16 shows several JES uncertainty hypotheses and how they effect the uncertainty on the search. With the standard 70 GeV jet energy threshold, the minimum value of E_{gluon} is 120 GeV. Since the uncertainty falls rapidly as E_{gluon} increases, variations in the reconstructed jet energy only impact deposits with energies close to the jet energy cut, which typically correspond to events in which E_{gluon} is small. We also conduct the analysis for increasing values of the JES uncertainty and determine that varying the uncertainty up to $\approx$45% has no significant impact on our limits.

Systematic uncertainties are summarized in Table 5.6.

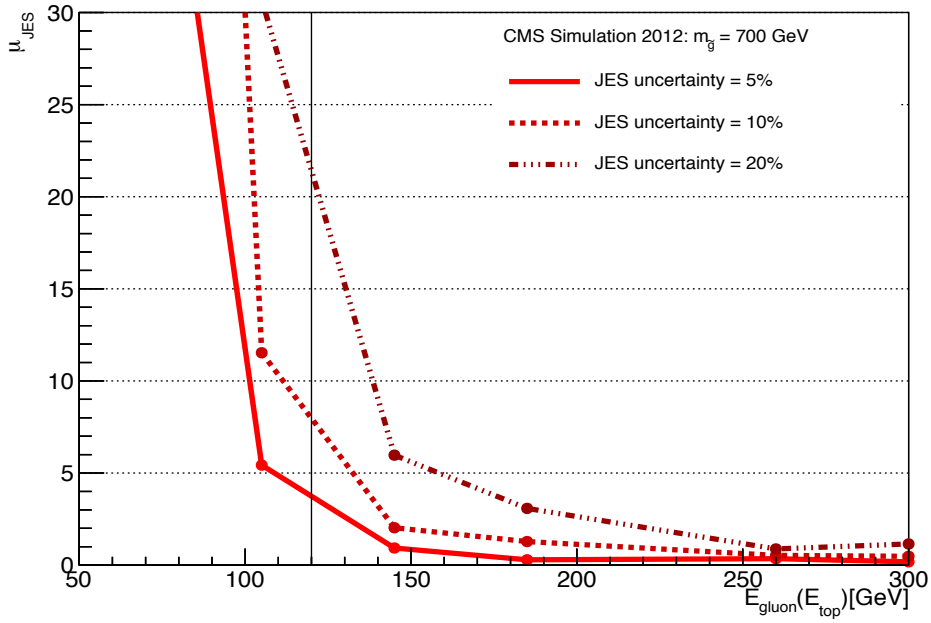

Figure 5.16: The systematic uncertainty(μ_{JES}) on the limits due to JES uncertainties of 5%, 10%, 20% for a variety of gluon energies. Using a jet energy threshold of 70 GeV, we require E_{gluon} >120 GeV.

5.8 Search Results and 95% C.L. Exclusion Limits on Gluino and Stop Production

The total and individual background estimates for both the 2012 search period and the 2010 control period, which is used to determine the noise background, are summarized in Table 5.7, together with the number of observed events. In the 2012 search sample, we observe no significant excess over the expected background and so the results of the search are used to place limits on the production rates and masses of $\tilde{g}$ and $\tilde{t}$.

To calculate these limits, we perform a counting experiment over a set of lifetime hypotheses between 50 ns and 10^7 seconds. This range of lifetime hypotheses was chosen to represent the minimum lifetime we are sensitive to, which corresponds to 2

Table 5.6: Systematic uncertainties in the 2012 search

Sources of Systematic Error	Fractional Uncertainty
JES Uncertainty	3%
Luminosity Uncertainty	2.6%
RECO efficiency uncertainty (Section 5.5.5)	13%

Table 5.7: Summary of background predictions for the 2010 control and 2012 search

Period	Livetime (hrs)	Noise	Cosmics	Halo	Total	Observed
2010	253	$0.0^{+2.3}_{-0.0}$	4.8 ± 3.6	0.0 ± 0.0	$4.8^{+4.3}_{-3.6}$	2
2012	281	$0.0^{+2.6}_{-0.0}$	5.2 ± 2.5	8.0 ± 0.4	$13.2^{+3.6}_{-2.5}$	10

BX after a collision, and the maximum lifetime for which we could reasonably expect CMS to record decays given the duration of uninterrupted run time. We assume the backgrounds predicted in Table 5.7 are uniformly distributed in time, which is a good approximation over the full dataset, despite short fluctuations in the beam halo rates within fills.

The counting experiment goes as follows: for each lifetime hypothesis, τ, the number of expected background events and qualifying selected events is determined based on how the structure of the protons beams affects our sensitivity to decays with that lifetime. We mask out periods during which the trigger is active but are so long after a pp collision that a decay occurring would be extremely unlikely. If a trigger period is more than $\tau \times 1.256$ from the previous collision, it's not included in the counting experiment. The sum of remaining unmasked time is our effective livetime for τ. This value is multiplied by the background rate gives the number of expected background events.

The next step is to consider which of the selected events could correspond to the chosen value of τ. If we are testing a short lifetime hypothesis, but the selected event occurs long after ($\tau \times 1.256$) the most recent collision event, this event is discounted. Note that for long lifetimes, no selected events are discounted.

Finally, we use the toy MC described in described in Section 5.4.1 to calculate the effective luminosity (L_{eff}). Table 5.8 shows the results of the counting experiment for several lifetime hypotheses.

Table 5.8: Results of counting experiments for selected lifetime hypotheses

Lifetime	$L_{eff}(fb^{-1})$	Live time (s)	Expected bkg	Observed
50ns	0.121	5.0×10^4	$0.66^{+0.18}_{-0.07}$	0
75ns	0.271	1.0×10^5	$1.3^{+0.4}_{-0.2}$	3
100ns	0.512	2.0×10^5	$2.6^{+0.7}_{-0.5}$	3
$1\mu s$	2.864	8.4×10^5	$11.0^{+3.0}_{-2.1}$	6
$10\mu s$	3.885	1.0×10^6	$13.1^{+3.6}_{-2.4}$	10
$100\mu s$	3.972	1.0×10^6	$13.2^{+3.6}_{-2.5}$	10
$10^3 s$	3.868	1.0×10^6	$13.2^{+3.6}_{-2.5}$	10
$10^4 s$	3.004	1.0×10^6	$13.2^{+3.6}_{-2.5}$	10
$10^5 s$	1.727	1.0×10^6	$13.2^{+3.6}_{-2.5}$	10
$10^6 s$	1.181	1.0×10^6	$13.2^{+3.6}_{-2.5}$	10

5.8.1 Limits on Gluino and Stop Production

Limits on the cross sections for $\tilde{g}$ and $\tilde{t}$ are obtained by performing the counting experiment described above and inputting the results into a CLs limit calculator. This calculation uses assumes a normally distributed background, which is randomly sampled based on the expected background and associated uncertainty. Using a Poisson distribution, we then iterate over a series of signal hypotheses to determine

the maximum possible signal allowed, assuming a 95% CL. The resulting value of the number of signal events is then used to calculate limit on the cross section for $\tilde{g}$ and $\tilde{t}$ pair-production, using the value of the effective luminosity calculated previously.

Limits using 2012 data with center of mass energy of 8 TeV as a function of lifetime are shown in Figure 5.17. The left hand axes give cross section limits assuming minimum energies of the decay products: $E_{gluon} > 120$ GeV and $E_{top} > 150$ GeV. These energies requirements are set by determining the point at which the reconstruction efficiency becomes constant (Section 5.5.5). Of particular note is the fact that these limits apply even for decays when the resulting top quark is off-shell, provided that its total energy is above the minimum threshold.

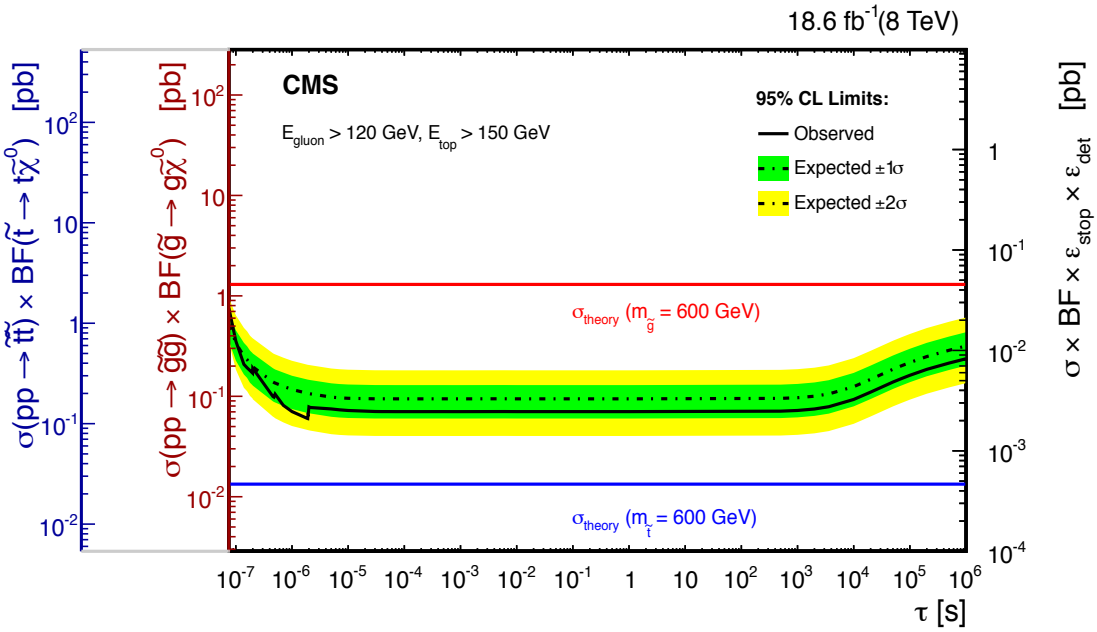

Figure 5.17: Expected and observed 95% C.L. limits on $\tilde{g}$ and $\tilde{t}$ pair production cross-sections. The theoretical cross-sections used in this calculation are taken from [1]. When $E_{top} < m_{top}$, the top quark is allowed to go off-shell.

5.8.2 Limits on Gluino and Stop Mass

Using the NLO+NLL SUSY particle production cross-sections from [1], we are also able to place limits on the masses of $\tilde{g}$ and $\tilde{t}$. Figure 5.18 shows these results. Over a lifetime range of 1 μs < τ <1000 s with E_{gluon} >120 GeV and E_{top} > 150 GeV, we exclude gluinos with $m_{\tilde{g}} < 880$ GeV/c^2 and stops with $m_{\tilde{t}} < 470$ GeV/c^2 at 95% C.L. Because of the requirements on the minimum energies for the gluon(top), these limits do not apply for all neutralino masses.

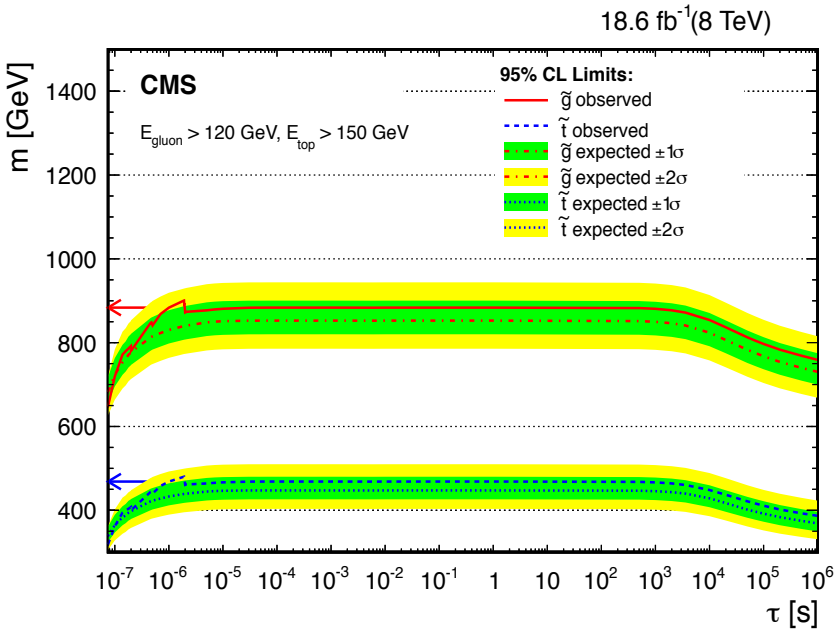

Figure 5.18: Expected and observed 95% C.L. limits on $m_{\tilde{g}}$ and $m_{\tilde{t}}$ pair production cross-sections. The theoretical cross-sections used in this calculation are taken from [1]. When $E_{top} < m_{top}$, the top quark is allowed to go off-shell.

5.8.3 Results Obtained with Higher Energy Thresholds

In the maturation process of this analysis, we focus primarily on developing our offline selection cuts to reduce our background contamination at low energies, and then are able to be more aggressive with the removal of backgrounds by increasing the jet energy threshold. Since ϵ_{RECO} is essentially flat above the minimum energy of $E_{gluon}(E_{stop})$, and the background falls steeply with energy, we can obtain stronger limits on the production cross-section by running the analysis with an increased jet energy threshold. This more aggressive method of reducing background was performed for thresholds of 100, 150, 200, and 300 GeV. However, as the jet energy threshold increases, our sensitivity to decays with very heavy $\tilde{\chi}^0$ degrades. If there is a smaller mass-splitting between $\tilde{g}(\tilde{t})$ and $\tilde{\chi}^0$, the amount of energy available for the visible decay product is small.

To perform the analysis at the higher jet energy thresholds, the higher energy threshold is first applied to the signal Monte Carlo to calculate the minimum energy of $E_{gluon}(E_{stop})$ and ϵ_{RECO} for each threshold. Next, we repeat the analysis of the 2010 data to estimate the noise rate at increased threshold, and then the cosmic and beam halo rates are determined in the same manner as for the 70 GeV analysis. We determine limits on cross-section, gluino, and stop masses, as described above. The cross-sections are presented in Figure 5.20. The mass limits for each threshold (Figure 5.21) are valid for a minimum value of $E_{gluon}(E_{stop})$, which we calculate from the turn-on curves shown in Figure 5.19. The minimum values of $E_{gluon}(E_{stop})$ for each threshold are listed in Tables 5.10 and 5.11. These values must increase with the increased jet energy threshold because the turn on curve for ϵ_{RECO} changes with the higher thresholds.

The systematic uncertainties on ϵ_{RECO} and luminosity are unaffected by the in-

crease in the jet energy threshold. However, the uncertainty resulting from the JES systematic does vary somewhat with different thresholds. The final JES uncertainty is calculated by measuring the change in ϵ_{RECO} when the jet energy threshold cut is varied according to the JES systematic. Variations in the jet energy cut have the largest impact for gluon (stop) energies right at the threshold, so we perform this calculation on signal Monte Carlo corresponding to the minimum values of E_{gluon} (E_{top}). When the separation between E_{gluon} (E_{top}) and the jet energy cut is small, the effect of the JES systematic increases.

As mentioned previously, increasing the jet energy threshold affects the masses of $\tilde{\chi}^0$ that are accessible to the analysis. Figure 5.22 summarizes how these different jet energy thresholds exclude different regions of the $(m_{\tilde{g}}, m_{\tilde{\chi}^0})$ phase space. Figure 5.23 does the same for the $(m_{\tilde{t}}, m_{\tilde{\chi}^0})$ phase space, though it only applies to on-shell top decays due to the fact that it is not possible to explicitly calculate $m_{\tilde{\chi}^0}$ when the top goes off-shell. It should be noted that the minimum lifetime for the higher threshold limits increases from 1 μs to 10 μs. This decrease in sensitivity to smaller lifetimes is due to the lower statistics associated with the increased energy cut.

Table 5.9: Detailed background estimates and systematics for varying energy thresholds.

Threshold (GeV)	$N_{bkg,noise}$	$N_{bkg,cosmic}$	$N_{bkg,halo}$	$N_{bkg,TOTAL}$
70	$0.0^{+2.6}_{-0.0}$	5.2 ± 2.5	8.0 ± 0.4	$13.2^{+3.6}_{-2.5}$
100	$0.0^{+2.0}_{-0.0}$	3.1 ± 1.2	1.7 ± 0.4	$4.9^{+2.4}_{-1.2}$
150	$0.0^{+2.2}_{-0.0}$	1.6 ± 1.0	0.6 ± 0.1	$2.1^{+2.4}_{-1.0}$
200	$0.0^{+1.3}_{-0.0}$	0.5 ± 0.4	0.5 ± 0.1	$0.7^{+1.4}_{-0.4}$
300	$0.0^{+1.3}_{-0.0}$	0.4 ± 0.4	0.04 ± 0.02	$0.4^{+1.3}_{-0.4}$

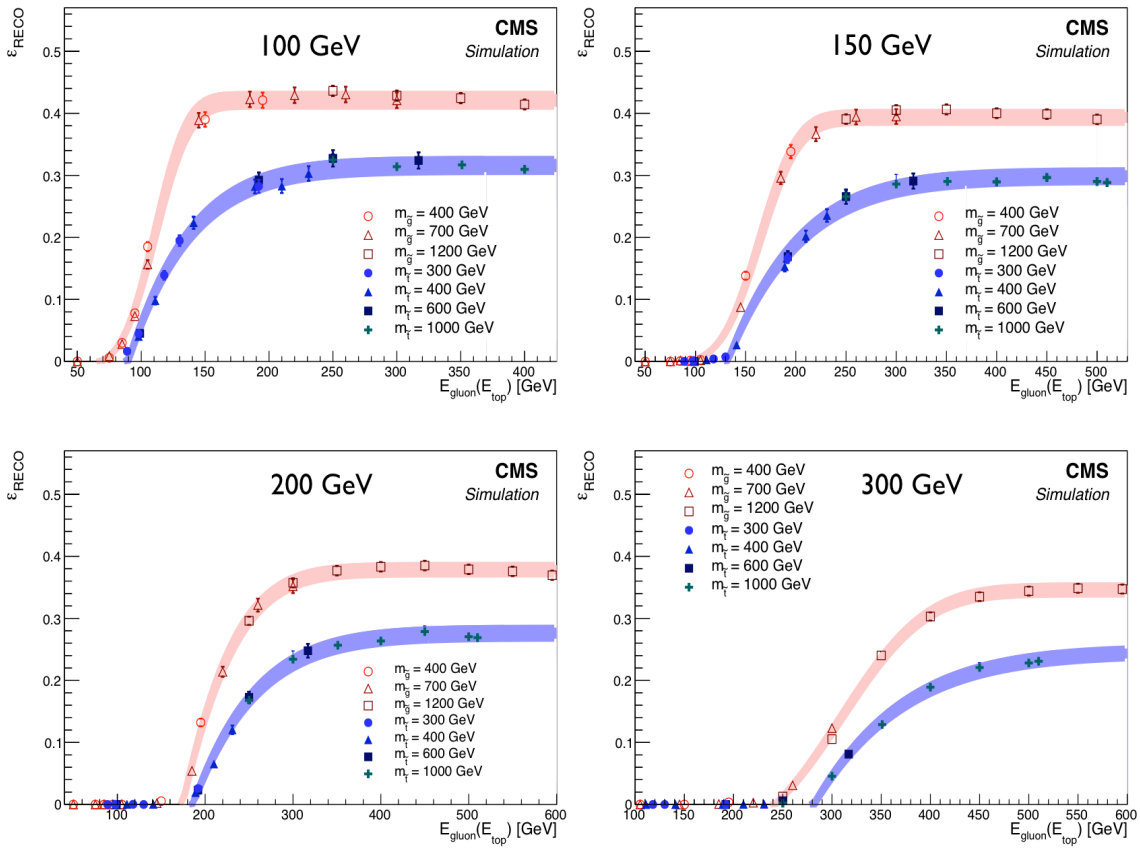

Figure 5.19: ϵ_{RECO} for $\tilde{g}$ and $\tilde{t}$ R-hadrons that stopped in EB or HB as a function of produced the energy of the SM daughter particle for 100, 150, 200, and 300 GeV energy thresholds.

5.9 Conclusion

The results of the search for long-lived, stopped particles at CMS have been presented here. Using a custom trigger to examine events that occur outside of proton-proton collisions, we have been able to substantially reduce the backgrounds, leaving only beam halo, cosmic rays, and instrumental noise. We are also able to search for very long-lived particles that decay with a hadronic component in the decay products. Over the course of leading this analysis, I have successfully developed new and more sophisticated techniques for discriminating against cosmic ray and instrumental noise

Table 5.10: Results of the analysis with varying energy thresholds for $\tilde{g}$

Threshold (GeV)	E_{gluon}^{min}	N_{bkg}	N_{obs}	$m_{\tilde{g}}$ limit
70	120	$13.2^{+3.6}_{-2.5}$	10	880
100	150	$4.9^{+2.4}_{-1.2}$	1	990
150	220	$2.1^{+2.4}_{-1.0}$	0	1010
200	320	$0.7^{+1.4}_{-0.4}$	0	1020
300	430	$0.4^{+1.3}_{-0.4}$	0	1020

Table 5.11: Results of the analysis with varying energy thresholds for $\tilde{t}$

Threshold (GeV)	E_{top}^{min}	N_{bkg}	N_{obs}	$m_{\tilde{t}}$ limit
70	150	$13.2^{+3.6}_{-2.5}$	10	470
100	200	$4.9^{+2.4}_{-1.2}$	1	530
150	300	$2.1^{+2.4}_{-1.0}$	0	550
200	360	$0.7^{+1.4}_{-0.4}$	0	550
300	470	$0.4^{+1.3}_{-0.4}$	0	550

backgrounds. Successes with the latter of these has resulted in increasing the trigger livetime, which will be crucial in future LHC run periods when the spacing between collisions will decrease to 25 ns. I also significantly improved the methods used to estimate the rate of each of the backgrounds that may escape our selection cuts.

No excess above the expected background was observed. Using a combination of a counting experiment and toy MC, we are able to place upper limits on both the cross section and the mass of supersymmetric particles, specifically the gluino and the stop. Using 281 hours of 8 TeV data taken in 2012, corresponding to 18.6 fb^{-1}, we excluded gluinos with $m_{\tilde{g}} < 880$ GeV that decay with BR($\tilde{g} \to g\tilde{\chi}^0$) = 100% for $E_{gluon} > 120$ GeV. We also exclude stops with $m_{\tilde{t}} < 470$ GeV assuming BR($\tilde{t} \to t\tilde{\chi}^0$) = 100% with $E_{top} > 150$ GeV. These limits apply over a large range of lifetime

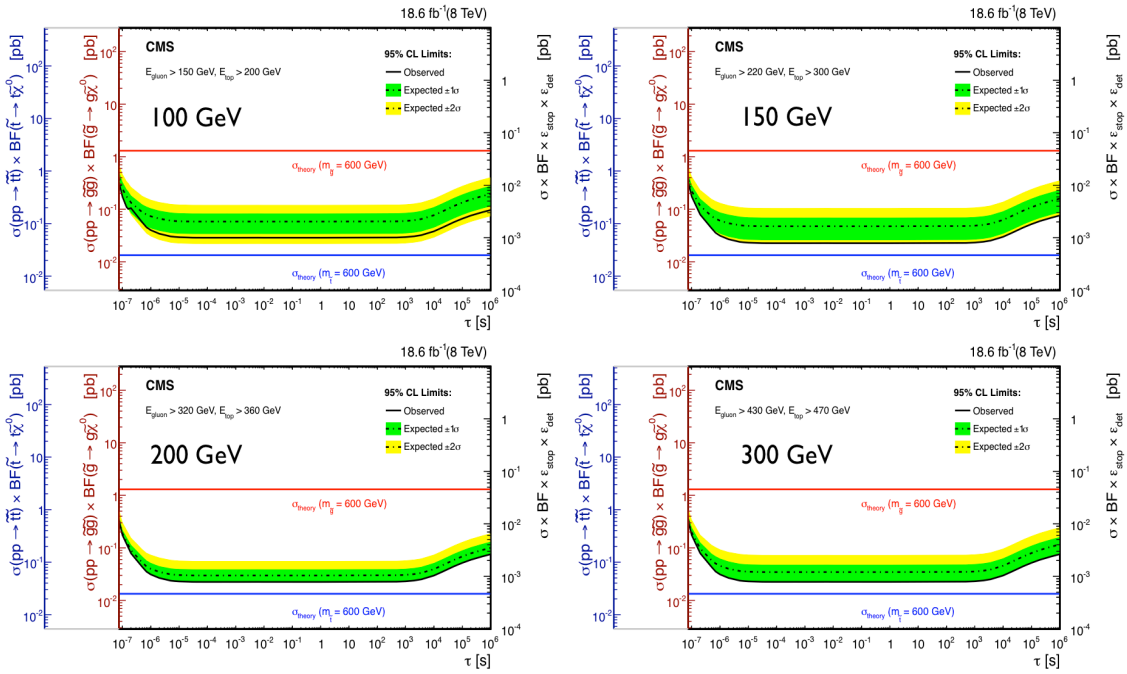

Figure 5.20: Expected and observed 95% C.L. limits on stop and gluino pair production cross-section for 100, 150, 200, and 300 GeV thresholds. When $E_{top} < m_{top}$, the top quark is allowed to go off-shell.

hypotheses, from 1 μs to 1000 s. In addition to these results, we also increase the minimum jet energy thresholds which decrease the background contamination, with the trade-off of sensitivity to higher mass $m_{\tilde{\chi}^0}$. This increase in energy thresholds allow for higher mass limits. These limits are the most stringent to date for a search of this type.

This analysis will continue in future LHC run periods, starting when proton-proton collisions begin in Spring of 2015. There is still great potential to develop future iterations of the analysis. The most promising extension of the current search is a shape-based analysis that could discriminate between a small number of potential signal events and possible background contamination by comparing the energy distributions of the recorded jets. The signal and backgrounds have both qualitative

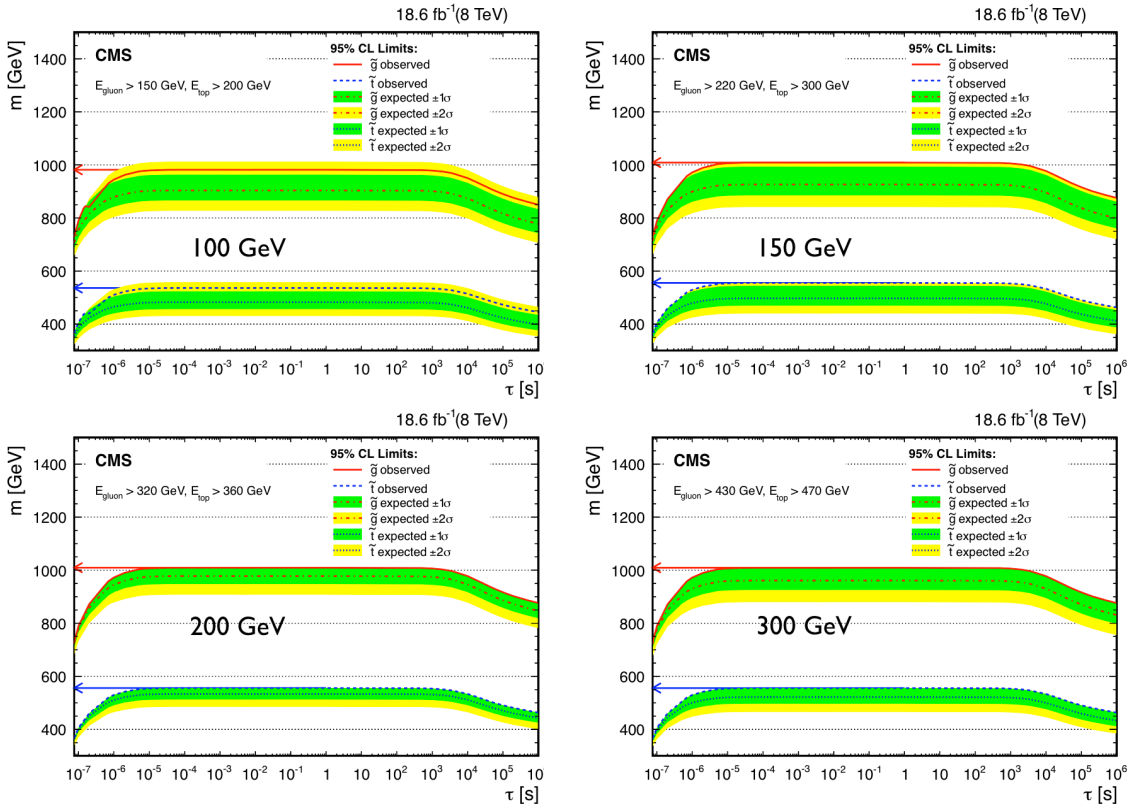

Figure 5.21: Expected and observed 95% C.L. limits on stop and gluino masses for 100, 150, 200, and 300 GeV thresholds. When $E_{top} < m_{top}$, the top quark is allowed to go off-shell.

and quantitative differences in the energy distributions, making this an exciting possibility. All three of the primary backgrounds have energy distributions that fall off rapidly above the trigger threshold, but signal events with a significant splitting between $m_{\tilde{\chi}^0}$ and $m_{\tilde{g}}$ ($m_{\tilde{t}}$) would be observed as an approximately normal distribution with a mean energy easily distinguished from the backgrounds. In addition to that, as beam related backgrounds, specifically beam halo, increase, further development on the background discrimination algorithms will likely be necessary. Of particular interest is exploiting differences between signal and beam halo in the characteristics of their HCAL deposits. I have previously explored this avenue but there is much more

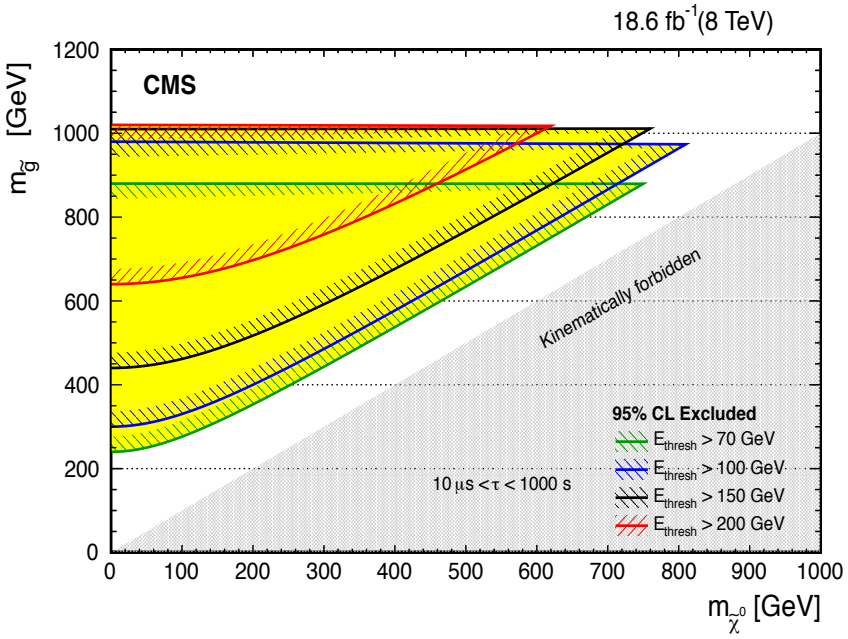

Figure 5.22: Region of the $m_{\tilde{g}} - m_{\tilde{\chi}^0}$ plane excluded by the analysis, valid for 10^{-5} s$< \tau_{gluino} < 10^3$ s using several energy thresholds.

work to be done. Applying this analysis in 2015 when the center of mass collision energy will be 13.8 TeV will continue to provide a unique look into potential signs of new physics beyond the Standard Model.

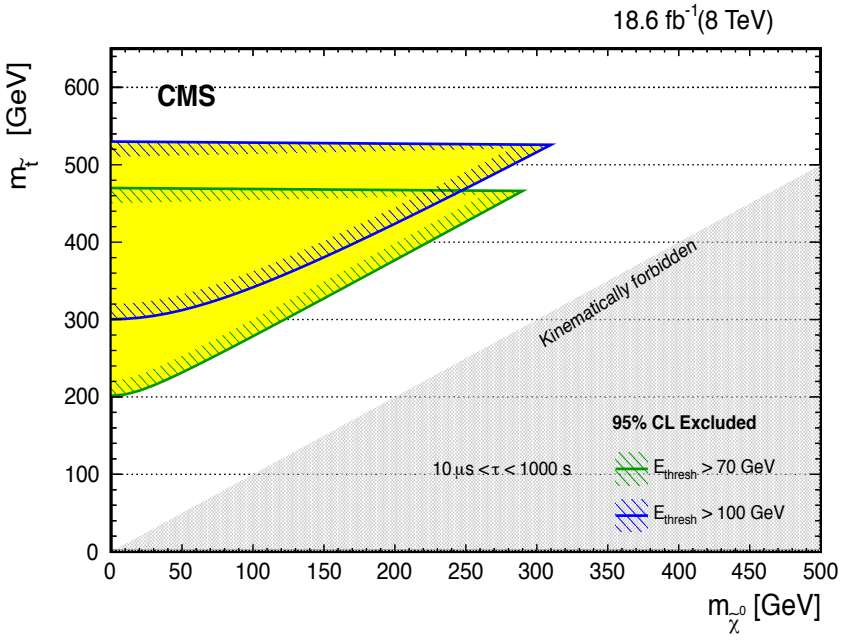

Figure 5.23: Region of the $m_{\tilde{t}} - m_{\tilde{\chi}^0}$ plane excluded by the analysis, valid for $10^{-5}s < \tau_{stop} < 10^{3}s$ using several energy thresholds. NOTE: the excluded region only applies to on-shell tops. In the case of off-shell tops, there is not enough information to calculate the value of $m_{\tilde{\chi}^0}$.

Bibliography

[1] Kramer, M., Kulesza, A., van der Leeuw, R., Mangano, M., Padhi, S., Plehn, T., and Portell, X. Supersymmetry production cross sections in pp collisions at $\sqrt{s} = 7$ TeV. Technical Report arXiv:1206.2892. CERN-PH-TH-2012-163, , Jun (2012). Cited on pages xi, 71, and 72.

[2] CMS Collaboration. "Observation of a new boson at a mass of 125 GeV with the CMS experiment at the LHC". *Physics Letters B* **716**(1), 30 – 61 (2012). Cited on pages 2 and 8.

[3] ATLAS Collaboration. "Observation of a new particle in the search for the Standard Model Higgs boson with the ATLAS detector at the LHC". *Physics Letters B* **716**(1), 1 – 29 (2012). Cited on pages 2 and 8.

[4] Arkani-Hamed, N. and Dimopoulos, S. "Supersymmetric unification without low energy supersymmetry and signatures for fine-tuning at the LHC". *Journal of High Energy Physics* **2005**(06), 073 (2005). Cited on page 11.

[5] Evans, L. and Bryant, P. "LHC Machine". *Journal of Instrumentation* **3**(08), S08001 (2008). Cited on page 15.

[6] CMS Collaboration. "The CMS experiment at the CERN LHC". *Journal of Instrumentation* **3**(08), S08004 (2008). Cited on page 15.

[7] CMS Collaboration. "Energy calibration and resolution of the CMS electromagnetic calorimeter in pp collisions at $\sqrt{s} = 7$ TeV". *JINST* **8**, P09009 (2013). Cited on page 22.

[8] CMS Collaboration. Identification and mitigation of anomalous signals in CMS HCAL. Technical Report CMS-CR-2012-238, CERN, Geneva, , Sep (2012). Cited on page 22.

[9] CMS Collaboration. "Performance of CMS muon reconstruction in *pp* collision events at $\sqrt{s} = 7$ TeV". *JINST* **7**, P10002 (2012). Cited on page 26.

[10] CMS collaboration. "The performance of the CMS muon detector in proton-proton collisions at $\sqrt{s} = 7$ TeV at the LHC". *Journal of Instrumentation* **8**(11), P11002 (2013). Cited on page 26.

[11] "Mokhov, W. "Machine-induced backgrounds: their origin and loads on ATLAS/CMS". *FERMILAB-CONF–08-147-APC* **08**(147) (2008). Cited on page 30.

[12] CMS Collaboration. "Missing transverse energy performance of the CMS detector". *Journal of Instrumentation* **6**(09), P09001 (2011). Cited on page 32.

[13] Khachatryan, V. et al. "Search for Stopped Gluinos in pp collisions at $\sqrt{s} = 7$ TeV". *Phys. Rev. Lett.* **106**, 011801 (2011). Cited on page 37.

[14] CMS Collaboration. "Search for stopped long-lived particles produced in pp collisions at $\sqrt{s} = 7$ TeV". *Journal of High Energy Physics* **2012**(8), 1–32 (2012). Cited on page 37.

[15] ATLAS Collaboration. "Search for long-lived stopped R-hadrons decaying out-of-time with pp collisions using the ATLAS detector". *Phys.Rev.* **D88**(11), 112003 (2013). Cited on page 39.

[16] Sjostrand, T., Mrenna, S., and Skands, P. Z. "PYTHIA 6.4 Physics and Manual". *JHEP* **05**, 026 (2006). Cited on page 41.

[17] Sjostrand, T., Mrenna, S., and Skands, P. Z. "A Brief Introduction to PYTHIA 8.1". *Comput.Phys.Commun.* **178**, 852–867 (2008). Cited on page 41.

[18] Agostinelli, S. et al. "GEANT4: A simulation toolkit". *Nucl. Instrum. Meth.* **A506**, 250–303 (2003). Cited on page 41.

[19] Kraan, A. C. "Interactions of heavy stable hadronizing particles". *Eur. Phys. J.* **C37**, 91–104 (2004). Cited on page 41.

[20] Mackeprang, R. and Rizzi, A. "Interactions of coloured heavy stable particles in matter". *Eur. Phys. J. C* **50**, 353 (2007). Cited on page 41.

[21] Mackeprang, R. and Milstead, D. "An updated description of heavy-hadron interactions in GEANT4". *Eur. Phys. J C* **66**, 493 (2010). Cited on page 41.

[22] CMS Collaboration. "Performance of the CMS hadron calorimeter with cosmic ray muons and LHC beam data". *Journal of Instrumentation* **5**(03), T03012 (2010). Cited on page 66.

[23] Fitzgerald Schroeder, M. Performance of Jets in CMS. Technical Report CMS-CR-2014-065, CERN, Geneva, , May (2014). Cited on page 66.